

MR molecular imaging for monitoring and predicting tumor responses to immunotherapy

Victoria E. A. Laney¹, Walter Zhao¹, Inga Hwang¹, Emma Hampson¹, Juan Dong², Ryan C. Hall¹, Kristin Weber-Bonk³, Xueer Yuan¹, Elizabeth Delaney², Hannah Gilmore^{4,5}, Ruth Keri^{3,5}, Jordan Winter^{5,6}, Li Lily Wang^{2,5*} and Zheng-Rong Lu^{1,5,*}.

¹Department of Biomedical Engineering, Case Western Reserve University, Cleveland, OH 44106, USA

²Department of Translational Hematology and Oncology Research, Lerner Research Institute, Cleveland Clinic Foundation, Cleveland, OH 44106, USA

³Department of Cancer Biology, Lerner Research Institute, Cleveland Clinic Foundation, Cleveland, OH 44195, USA

⁴Department of Pathology, Cleveland Clinic Foundation, Cleveland, OH, 44195, USA

⁵Case Comprehensive Cancer Center, Case Western Reserve University, Cleveland, OH 44106, USA

⁶Department of Surgery, The University Hospitals of Cleveland, Cleveland, OH 44106, USA

Running head: MRMI for predicting the efficacy of immunotherapy

*Corresponding authors:

Zheng-Rong Lu, Ph.D.

M. Frank Rudy and Margaret Domiter Rudy Professor of Biomedical Engineering

Case Western Reserve University

Department of Biomedical Engineering, Wickenden 427

10900 Euclid Avenue, Cleveland, OH 44106

Phone: (216) 268-0187

Email: zx1125@case.edu

Li Lily Wang, PhD

Staff

Department of Translational Hematology and Oncology Research

Cleveland Clinic Foundation

Associate Professor of Molecular Medicine

Cleveland Clinic Lerner College of Medicine

NE5-217, Lerner Research Building

2111 East 96th Street

Cleveland, OH 44195

Phone: 216-973-5628

Email: wangl9@ccf.org

ABSTRACT

While immunotherapies show great promise in cancer treatment, variability in patient responses warrant the need for improved methods to assess early responses and guide precision therapy. The tumor microenvironment (TME) plays a critical role in antitumor immunity and tumor response to immunotherapy. Critically, TME constituents and their crosstalk with immune cells can be leveraged as a prognostic marker for therapeutic response. This study evaluated the use of magnetic resonance molecular imaging (MRMI) targeting the TME protein extracellular matrix (ECM) protein fibronectin (EDB-FN), which is a lymphokine secreted by activated T lymphocytes and a marker of epithelial-to-mesenchymal transition in aggressive tumor cells. MRMI of EDB-FN was evaluated within the tumor extracellular matrix and were correlated with immunotherapy-related outcomes.

Methods: C57BL/6 mice bearing orthotopic KPC pancreatic tumors were treated with a novel immune checkpoint inhibitor (VISTA-blocking antibodies), a vaccine (mutant KRAS-G12D peptide with TLR7/8/9 agonists), or a combination of both. MRMI with an EDB-FN-specific contrast agent, MT218, was used to image tumor responses during treatment. T₁-weighted MR images of the tumors were acquired before, during, and after treatment using fast spin echo and FLASH sequences. Signal enhancement patterns in the tumors were analyzed to assess tumor response to the treatments. EDB-FN expression and the infiltration of CD4⁺ and CD8⁺ T lymphocytes in the tumors were determined by immunohistochemistry and immunofluorescence staining, respectively, to correlate with MRMI observations, tumor responses, and therapeutic outcomes.

Results: MT218-MRMI revealed distinctive signal enhancement patterns across different treatments. These patterns were detected as early as two weeks after treatment initiation and correlated strongly with EDB-FN expression and CD4⁺ and CD8⁺ T cell infiltration, as confirmed by immunohistochemistry and immunofluorescence staining. The signal profiles corresponded to known TME phenotypes: immune desert, immune-excluded, and immune-inflamed, which were associated with non-response, partial response, and complete response, respectively. By four weeks post-treatment, MRMI criteria successfully distinguished complete responders from partial responders. Outcome prediction showed 100% long-term disease-free survival in complete

responders, 24-27% survival in partial responders, and no survival in non-responders or those with stable disease over a 200-day monitoring period.

Conclusion: The ability to distinguish response patterns using non-invasive MRMI with MT218 offers significant potential for early prediction of therapeutic outcomes and timely optimization of treatment strategies. While further validation of MT218-MRMI is needed for clinical translation, these findings demonstrate its promise as a tool for monitoring immunotherapy response in pancreatic cancer and underscore its potential impact on precision immunotherapy.

Keywords: MR molecular imaging, targeted MRI contrast agent, MT218, cancer immunotherapy, extradomain B fibronectin, therapeutic response

INTRODUCTION

Immunotherapy, including immune checkpoint inhibitors, has revolutionized cancer treatment, with improved survival outcomes across multiple solid tumor types [1]. Additionally, the introduction of anti-tumor vaccines, such as cancer-specific mRNA and neoantigen vaccines, has demonstrated a synergistic effect when combined with other immunotherapies [2-6]. However, individual patient responses remain heterogeneous, and therapeutic outcomes in many cancers are often suboptimal [7]. Furthermore, current diagnostic tools lack the accuracy needed to reliably distinguish responders from non-responders and predict treatment outcomes. As a result, non-responders may endure treatment-related side effects without therapeutic benefits and can lose opportunities to pursue alternative treatments. Therefore, there is a critical need for non-invasive, accurate, and accessible diagnostic and prognostic tools to monitor and predict tumor responses to immunotherapies.

Effective immunotherapies rely on lymphocyte activation and the recruitment of cytotoxic lymphocytes into cancerous tissues [2]. Impaired T cell responses to immunotherapy may result from insufficient infiltration and dysfunction of cytotoxic T lymphocytes. Beyond programmed death-1 (PD-1) and cytotoxic T-lymphocyte-associated protein 4 (CTLA-4), novel immune checkpoint receptors (ICRs) play non-redundant roles in suppressing anti-tumor T cell responses. Among these is the V-domain immunoglobulin suppressor of T cell activation (VISTA, gene *Vsir*) [8-10]. Previous studies have established that VISTA regulates anti-tumor immunity through multiple mechanisms, including promoting the metabolism and differentiation of myeloid-derived suppressor cells [11], impairing toll-like receptor (TLR) signaling and macrophage activation [12], and inhibiting anti-tumor T cell activation through cell surface protein, LRIG1, engagement [8, 9, 13-17]. VISTA blockade has been shown to reduce tumor growth in several preclinical tumor models [14, 15, 18, 19]. In human cancers, VISTA expression is detected on tumor-infiltrating myeloid cells and T cells and is associated with therapeutic resistance and recurrence [9, 20-23].

The tumor microenvironment (TME) plays a crucial role in anti-cancer immunity. It orchestrates tumor responses to immunotherapy and regulates immune cell infiltration, including cytotoxic T cells in solid tumors, thereby governing tumor responses to immunotherapy [24, 25]. The TME consists of the extracellular matrix (ECM), stromal cells, and immune cells. Based on

immune cell presence and distribution, the TME exhibits three distinct phenotypes: immune desert (absence of cytotoxic T lymphocytes), immune-excluded (peripheral presence without infiltration), and immune-inflamed (substantial infiltration). These phenotypes strongly correlate with immunotherapy response outcomes [26, 27]. Molecular imaging of these three phenotypes of TME has the potential to non-invasively monitor tumor response and predict therapeutic outcomes [28, 29].

Within the TME, the ECM regulates immune cell activation, differentiation, and infiltration [24, 25]. Fibronectin (FN), a key acellular component of the ECM, plays a crucial role in ECM assembly and organization while regulating cell adhesion, proliferation, and migration [30, 31]. As a marker of inflammation, tissue remodeling, and epithelial-mesenchymal transition (EMT) [32-35], FN also regulates T lymphocyte development, activation, migration, and proliferation [31, 36-40]. Extradomain B fibronectin isoform (EDB-FN) is an oncofetal subtype of FN and is overexpressed in aggressive human cancers, including pancreatic cancer, not in normal tissues, as shown by RNA-seq analysis and immunohistochemistry of human tissues [41-43]. It is a particularly valuable imaging target due to its overexpression in tumor ECMs, correlating with tumor grade and stage, while being minimally present in normal tissues [41, 42]. Moreover, EDB-FN is secreted by activated T cells ($CD4^+$ and $CD8^+$), establishing it as a lymphokine [44, 45], making it an ideal marker for real-time assessment of immunotherapy responses. Various imaging agents have been developed and tested for molecular imaging of EDB-FN for cancer detection and diagnosis [46-49]. However, EDB-FN has not been explored as a marker for immune activation.

We have developed a small peptide targeted MRI contrast agent ZD2-N3-Gd(HP-DO3A) (MT218) specific to EDB-FN for magnetic resonance molecular imaging (MRMI) of cancer [50]. Our approach uses MT218, a targeted contrast agent consisting of small peptide ZD2 (Thr-Val-Arg-Thr-Ser-Ala-Asp) conjugated with gadoteridol that specifically binds to the EDB fragment, **Figure 1A** [51]. As shown in our previous studies, EDB-FN is overexpressed in human PDAC tumors [41, 43]. MRMI with MT218 (MT218-MRMI) is effective detecting EDB-FN changes across multiple aggressive cancers, including breast, colorectal, head and neck, lung, prostate, and prostate cancers [52, 53]. Additionally, we have shown that MT218-MRMI can be used to monitor tumor progression and therapeutic responses in murine models [54-56]. These promising results

have led to an FDA-approved clinical trial (NCT06262139) evaluating MT218's tumor detection capabilities [57].

Here, we demonstrate how MT218-MRMI predicts tumor responses to three immunotherapeutic approaches in an orthotopic murine PDAC model: a VISTA-blocking mAb [15, 16], a peptide vaccine containing mutant KRAS^{G12D} peptide with adjuvants (R848 and CpG oligonucleotide, toll-like receptor 7/8/9 agonists) [5, 58, 59] and their combination. When effective, these therapies stimulate both innate and adaptive immune responses, leading to increased tumor-infiltrating T cells and enhanced EDB-FN secretion. As outlined in **Figure 1B**, MT218-MRMI enables early discrimination between treatment outcomes by detecting these changes. Our findings establish MT218-MRMI as a promising tool for non-invasive, high-resolution, longitudinal characterization of the dynamic TME, validating its utility for both diagnostic imaging and prognostic assessment in precision cancer immunotherapy.

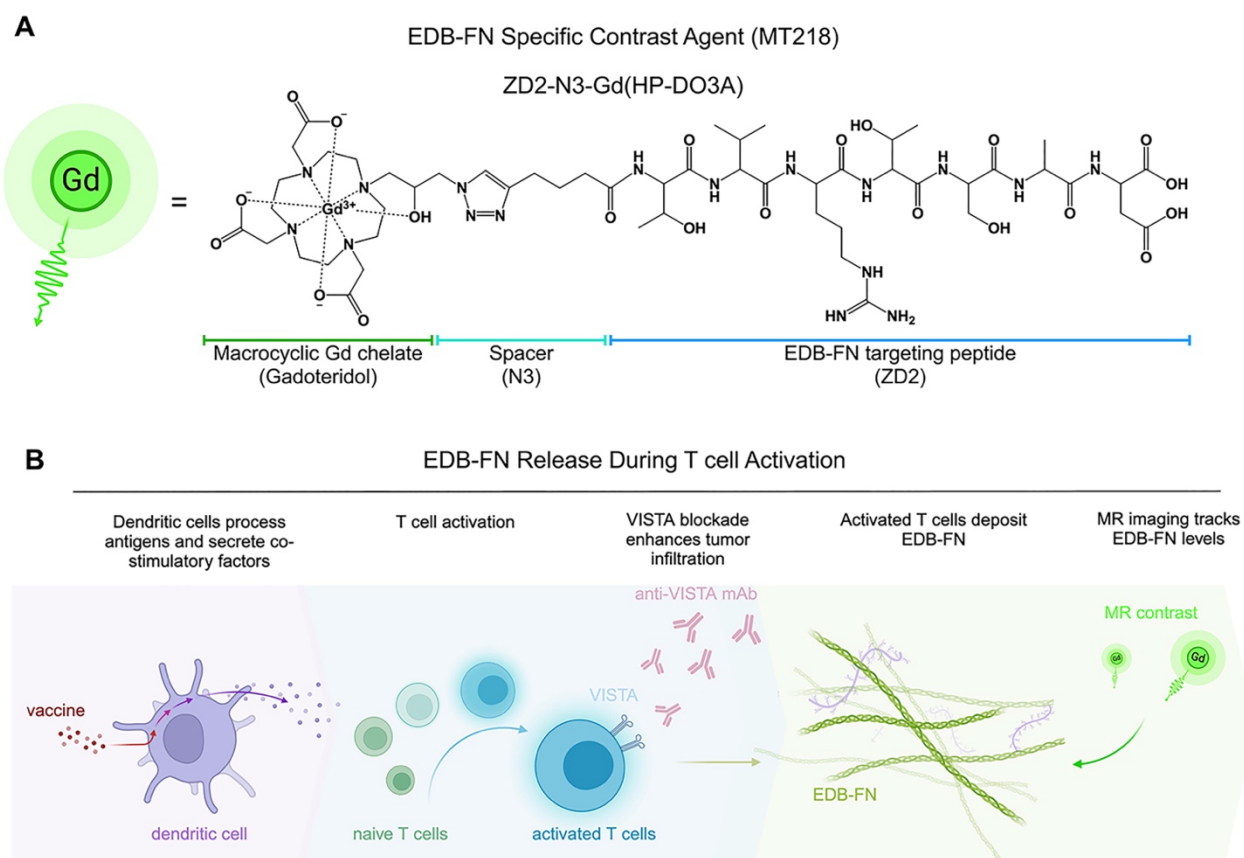


Figure 1. Conceptual overview of MT218-MRMI and its applicability to PDAC immunotherapy. **A)** Chemical structure of EDB-FN specific contrast agent, MT218 (right) and an illustrative representation (left). **B)** Activated T cells excrete and deposit EDB-FN as a form of immune-stromal crosstalk, which allows for MT218-MRMI to visualize EDB-FN expression to monitor the dynamic changes of the TME in response to immunotherapy.

RESULTS

MRMI for monitoring and prediction of tumor responses to anti-VISTA mAb therapy

To investigate how VISTA blockade influences immunotherapy-induced changes in the ECM and EDB-FN expression, we established an orthotopic PDAC model using KPC-K8484 cells implanted in immunocompetent C57BL/6 mice. Following the experimental schedule shown in **Figure 2A**, mice were treated with a VISTA-blocking monoclonal antibody (mAb). MT218-MRMI confirmed tumor establishment ten days after cell inoculation, with tumors clearly visible in axial slices adjacent to the spleen (**Figure 2B-D**). Administration of MT218 resulted in an overall signal increase within all tumors in T₁-weighted MR images, facilitating boundary detection and delineation of tumor masses from the pancreas.

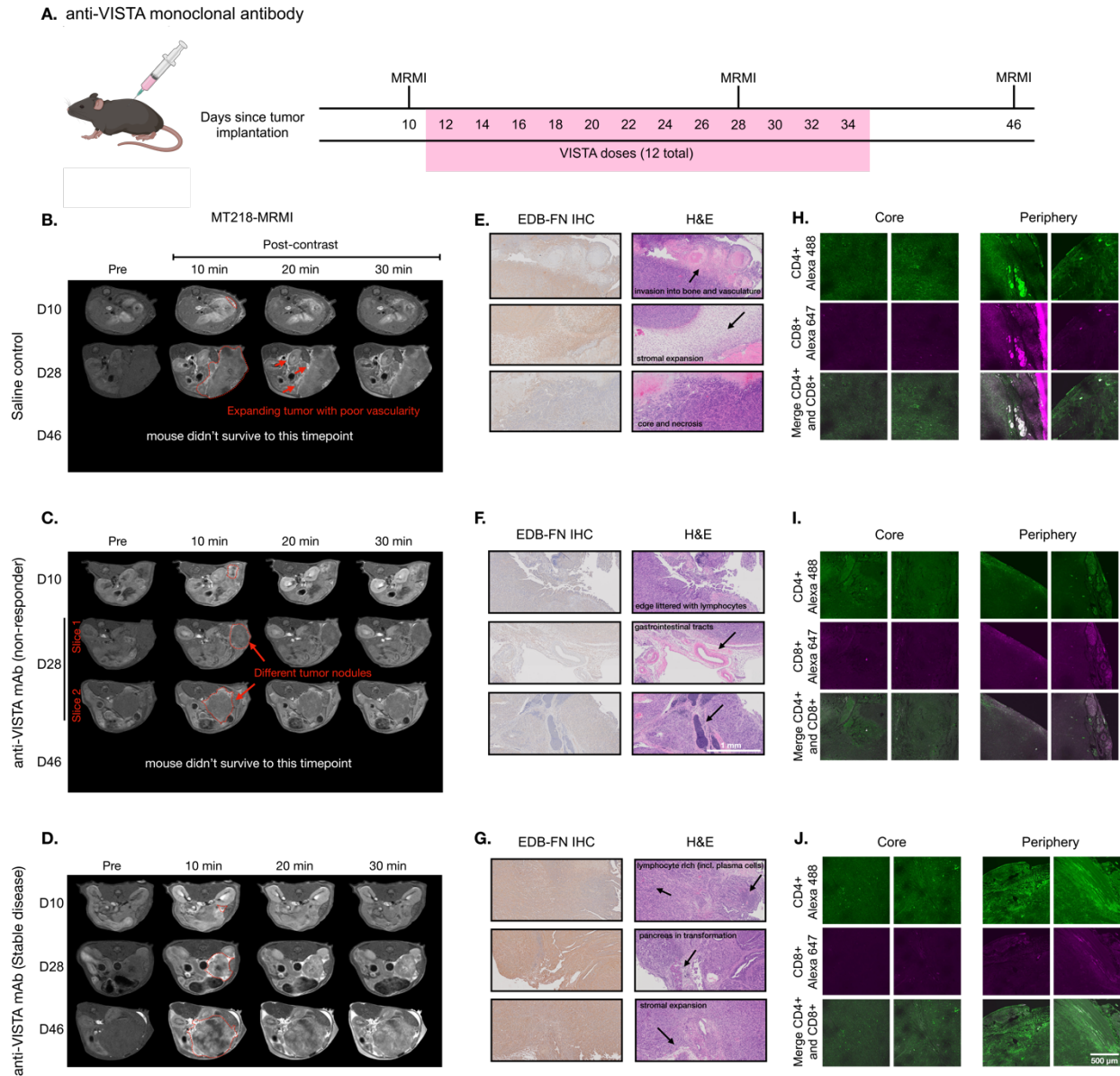


Figure 2. MT218-MRMI for monitoring tumor responses to anti-VISTA mAb in C57BL/6 mice bearing orthotopic KPC-K8484 allografts. **A)** Dosing and MRMI schedule for mice treated with VISTA blockade. **B-D)** Representative T_1 -weighted 2D fast spin-echo axial MRMI images of the mice treated with saline (**B**) and anti-VISTA mAb (**C**, non-responder; **D**, stable disease) before (Pre) and at 10, 20, and 30 min after intravenous injection of MT218 (0.1 mmol/kg, Post-contrast) on day 10, 28, and 46 after tumor initiation. Tumor is outlined with red dashed lines, areas of tumor expansion into abdominal tissues are indicated by red arrows. **E-G)** IHC of EDB-FN with anti-EDB G4 mAb and H&E staining of tumors from mice treated with saline (**E**) or anti-VISTA mAb (**F**, non-responder; **G**, stable disease) at the end of experiment. **H-J)** IF imaging of $CD4^+$ and $CD8^+$ T cells with an anti- $CD4^+$ mAb labeled with Alexa 488 (green) and an anti- $CD8^+$ labeled with Alexa 647 (magenta) in the tumors from the mice treated with saline (**H**) or anti-VISTA mAb (**I**, non-responder; **J**, stable disease).

Mice were treated either with saline (100 μ L, negative control) or an anti-VISTA monoclonal antibody (mAb, 200 μ g in 100 μ L) via intraperitoneal (i.p.) injection three times a week for a total of four weeks starting on day 12. T₁-weighted MT218-MRMI was then performed on days 28 and 46 to monitor tumor response and determine therapeutic efficacy. Non-contrast T₂-weighted MRI was also used to assess the disease progression of the tumors detected by MT218-MRMI. The average tumor sizes in various groups detected by MRI are shown in **Figure S1**. The MRI scans revealed disease progression in the control group, with lobular tumors exceeding 10% of body weight at endpoint. This aggressive phenotype was characterized by widespread metastasis (liver, kidney, spleen, bone, and muscle) in 63.2% of mice and a high rate of mortality, 75.9%, by day 46. Day 28 MRMI scans showed heterogeneous enhancement patterns across tumor masses, **Figure 2B**. These findings, supported by tumor growth curves (**Figure S1**) established the baseline parameters for assessing treatment response in subsequent therapeutic experiments.

In comparison, anti-VISTA mAb elicited heterogeneous responses among treated mice. Outcomes were characterized by the size of the primary tumor, presence of metastatic tumors and post-contrast signal enhancement pattern. Of the 14 treated mice (6 female, 8 male), eight exhibited a non-responder phenotype, with large tumors with low contrast enhancement comparable to controls and widespread metastases (**Figure 2C**). These non-responders had poor survival, with 87.5% not surviving to the third MRMI scan planned for day 46. In contrast, six mice demonstrated stable disease (SD), characterized by smaller tumors compared to controls, no detectable metastases, and distinctly brighter signal enhancement on days 28 and 46 (**Figure 2D**). This group showed markedly improved survival, with 83.3% surviving to day 46.

Assessment of MT218-MRMI of the SD mice showed brighter signal enhancement in tumor periphery and moderate signal in the tumor core on day 28 and 46, indicative of augmented EDB-FN expression within these tumors. Quantitative analysis showed MT218 produced a 3-6-fold increase in average normalized contrast-to-noise ratios (CNR) across all tumors compared to pre-treatment (day 10, **Figure S2**). Notably, SD tumors exhibited significantly higher CNR increases (6.17- and 5.75-fold at 10- and 20-min post-contrast) on day 28 compared to both controls (3.64- and 3.51-fold) and non-responders (3.44- and 2.82-fold). To validate that enhanced signals resulted from specific binding rather than passive diffusion, we compared MT218 to non-targeted

gadoteridol in the SD tumors after treatment (**Figure S3**) confirming that increased enhancement was due to specific EDB-FN binding of MT218.

Histological analyses were performed at days 28 and 46 (post-MRMI) or at humane endpoint comprehensively characterized treatment responses. Immunohistochemistry (IHC) using anti-EDB-FN (G4) mAb revealed distinct staining patterns of EDB-FN expression in the tumors across treatment groups: control tumors showed heterogeneous, moderate EDB-FN staining (**Figure 2E**) non-responding tumors displayed relatively weak staining throughout (**Figure 2F**) and the SD tumors exhibited strong staining, particularly intense in the tumor periphery compared to the core, **Figure 2G**. These EDB-FN expression patterns, both in intensity and spatial distribution, corroborated the MT218-MRMI signal patterns.

Hematoxylin and eosin (H&E) staining revealed distinct histopathological features among treatment groups. Control and non-responding tumors showed dense adenocarcinoma with minimal pancreatic tissue remnants and little core necrosis, **Figure 2E, F**. These tumors exhibited aggressive behavior, with direct lymphatic invasion and expansion into surrounding tissues including lymph nodes, skeletal muscle, liver, and bones. In contrast, SD tumors had areas of dense adenocarcinoma, and also showed substantial core necrosis and retained some pancreatic tissue architecture (**Figure 2G**).

T cell infiltration patterns in the tumors determine the tumor immune microenvironment (TIME) phenotypes in response to immunotherapy, and these can be used in tandem with other prognostic factors to predict therapeutic response. In our pilot experiments, flow cytometry is limited to provide the infiltration patterns of immune cells in the tumors. Therefore, we performed immunofluorescence imaging (IF) to determine the infiltration patterns of T cells in the tumors in responding to immunotherapy. Confocal immunofluorescence imaging revealed that control treated tumors showed the presence of CD4⁺ T cells throughout the tumors but cytotoxic CD8⁺ T cells restricted to the periphery (**Figure 2H**). Non-responding tumors displayed minimal infiltration of both CD4⁺ and CD8⁺ T cells (**Figure 2I**), characteristics of an immune desert phenotype. The SD tumors exhibited substantial CD4⁺ T cell presence, particularly at the tumor periphery, with CD8⁺ T cells similarly restricted to peripheral regions (**Figure 2J**) indicating an

immune-excluded phenotype. Healthy pancreases were also imaged to establish a baseline for normal mice pancreas tissue (**Figure S4**).

We also examined the correlation of MT218-MRMI with the TME phenotypes in the tumors determined by immunofluorescence analysis on day 28 after 2 weeks of treatment with saline or anti-VISTA mAb. Response assessment at day 28 revealed that 50% of anti-VISTA mAb-treated mice displayed heterogeneous bright signal enhancement without metastases (**Figure 3A**). SD tumors showed distinctive enhancement patterns, with bright signals in both core and rim regions. Corresponding histological analyses confirmed enhanced EDB-FN expression and reduced cell density in SD tumors compared to non-responders, **Figure 3B**, validating the MT218-MRMI data (**Figure S5**), particularly at a timepoint two weeks post-treatment initiation.

Immunofluorescence imaging revealed distinct T cell infiltration patterns that correlated with treatment response. SD tumors exhibited substantial CD4⁺ and CD8⁺ T cell presence at the tumor periphery, with only CD4⁺ T cells detected in the core (**Figure 3C**). In contrast, non-responding tumors contained sparse CD4⁺ T cells and lacked CD8⁺ T cells that are essential for cytotoxic activity in antitumor immunotherapy [60, 61]. These cellular patterns aligned with MT218-MRMI signal characteristics: SD tumors displayed bright rim enhancement with moderate core signals, reflecting an immune-excluded TME, while non-responders showed relatively weaker periphery enhancement and weak core enhancement, consistent with an immune desert TME. We determined the correlation between immunofluorescence (IF) staining of CD4 and CD8 markers and MRMI signal measurement in the treated tumors (**Figure S6**). Although MRMI could not distinguish CD4⁺ vs CD8⁺ T cells in the tumors, MRMI signal was correlated with the overall abundance of activated T cells in the tumors in various treatment groups. Both MRMI and T cell staining showed that anti-VISTA antibody treatment caused an enhanced CD4⁺ T cell infiltration within the tumor core regions in SD hosts. This correlation indicates that MT218-MRMI may reliably detect the different TIME types that is correlated with distinct therapeutic response to anti-VISTA treatment.

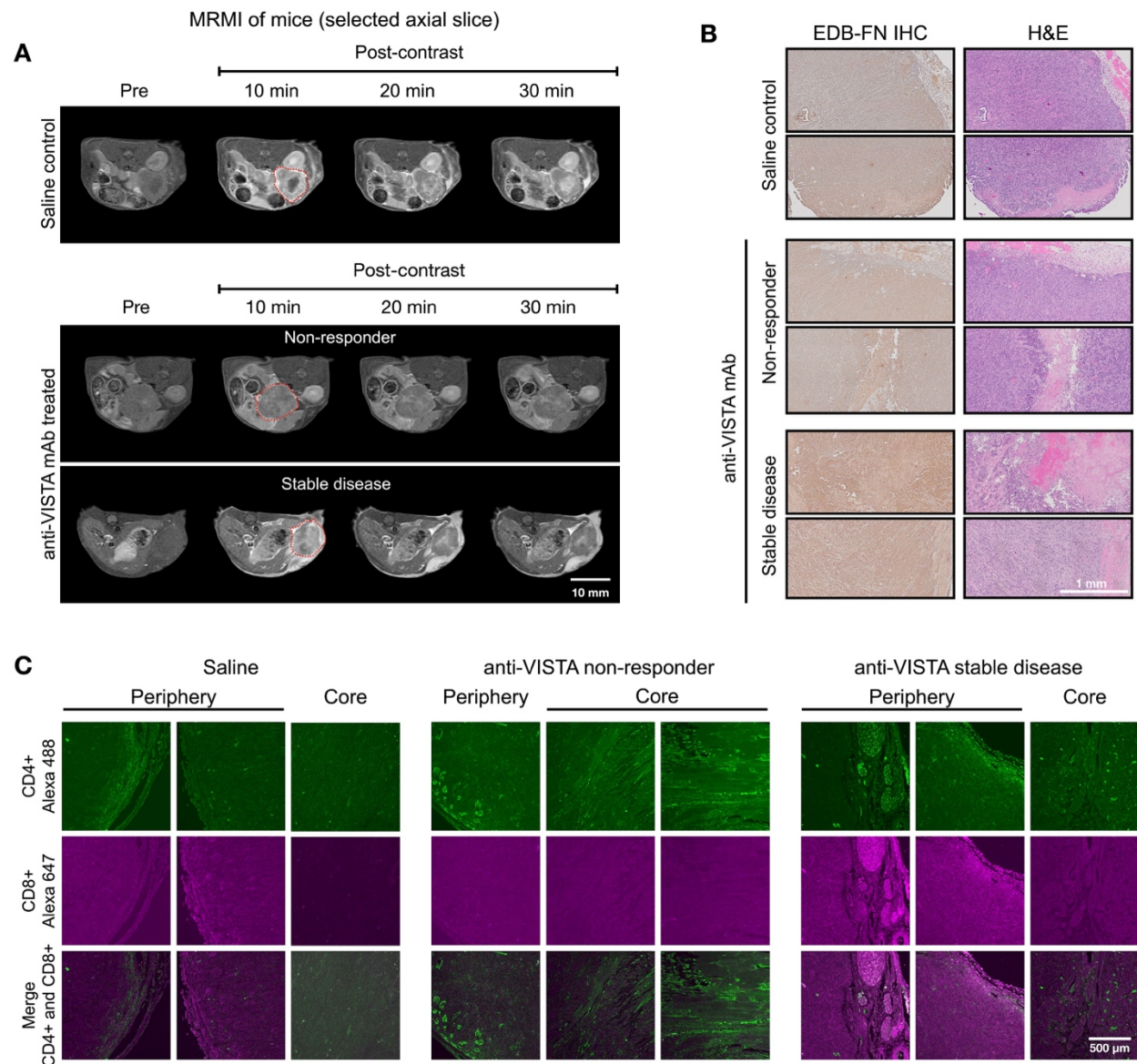


Figure 3. MT218-MRMI for monitoring early tumor response to anti-VISTA mAb in C57BL/6 mice bearing orthotopic KPC-K8484 allografts. A) Representative T₁-weighted 2D fast spin-echo axial MRMI of tumors (red dashed lines) of the mice dosed with either saline or anti-VISTA mAb. Mice were imaged before (Pre) and at 10, 20, and 30 min. after intravenous injection MT218 (0.1 mmol/kg, post-contrast) on day 28. **B)** IHC staining of EDB-FN in tumors with an anti-EDB mAb, G4 (left) and H&E staining (right) of the tumors. **C)** IF staining of CD4⁺ and CD8⁺ T cells with an anti-CD4⁺ mAb labeled with Alexa 488 (green) and an anti-CD8⁺ labeled with Alexa 647 (magenta) in the tumors.

MRMI for monitoring and predicting tumor response in response to a cocktail vaccine

In addition to VISTA inhibitor treatment, we investigated whether MT218-MRMI may predict the response to a different immunotherapy using neoantigen vaccine. Mice bearing orthotopic KPC tumors were treated with a cocktail of KRAS^{G12D}-derived peptide mixed with TLR agonists (R848 and CpG oligonucleotide). Following an initial vaccination on day 10 and a booster on day 17 (**Figure 4A**), tumor growth was significantly inhibited (**Figure S7**). MT218-MRMI identified three distinct response patterns in the treated tumors: non-responders (3/25 mice), which exhibited tumor growth comparable to the control group, with moderate tumor signal enhancement and metastases (**Figure 4C**); partial responders (12/25 mice), which showed reduced tumor growth with bright peripheral enhancement and weak core enhancement (**Figure 4D**); and complete responders (10/25 mice), which displayed bright signals throughout the tumors on day 28 and achieved complete tumor rejection by day 46 (**Figure 4E,F**).

Quantitative analysis showed significantly elevated CNR in complete responders by day 28 (6.46-fold vs pre-treatment 3.57-fold, **Figure S8**), while partial responders showed reduced enhancement (1.80 fold), and non-responders did not show significant change (3.64-fold vs 3.88-fold) at 10 min post-injection of MT218. Notably, the MRMI signal patterns by day 28 strongly predicted treatment outcomes, with 90% accuracy in identifying complete responders and 85% accuracy in distinguishing non-responders from partial responders. This predictive capability was validated through correlation with survival outcomes, where complete responders showed significantly improved survival (median survival >90 days) compared to partial responders (median survival 62 days) and non-responders (median survival 38 days) ($p < 0.001$).

A. KRAS^{G12D} vaccine

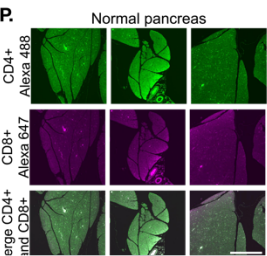
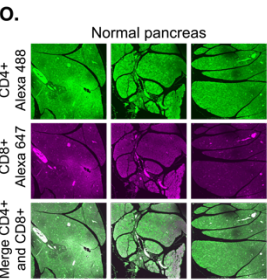
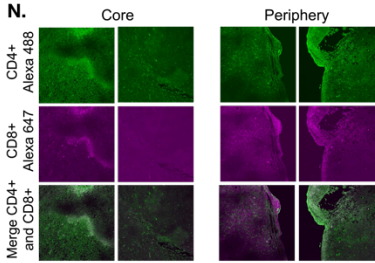
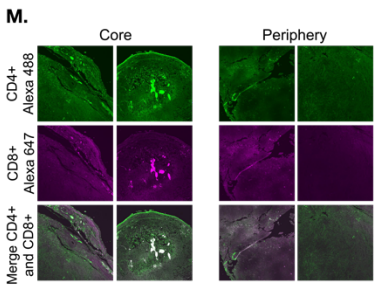
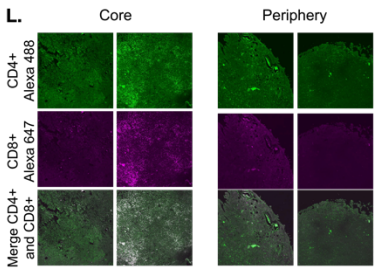
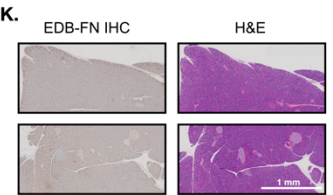
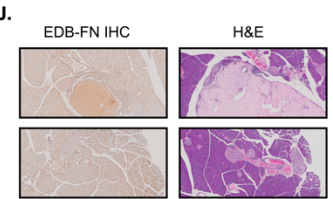
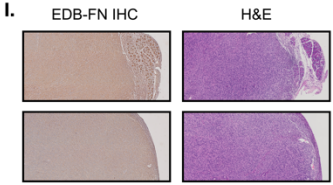
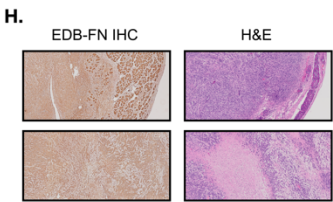
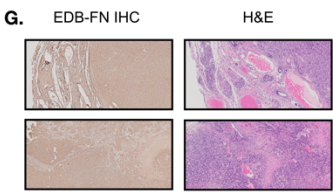
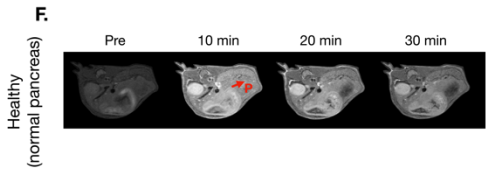
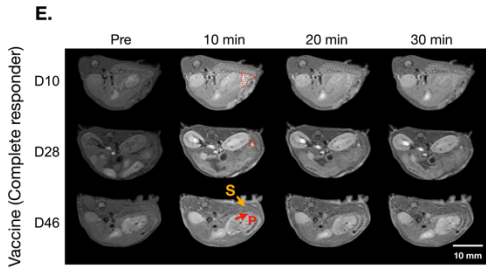
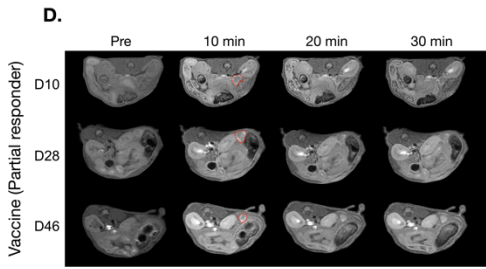
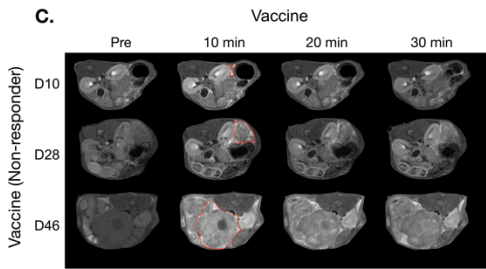
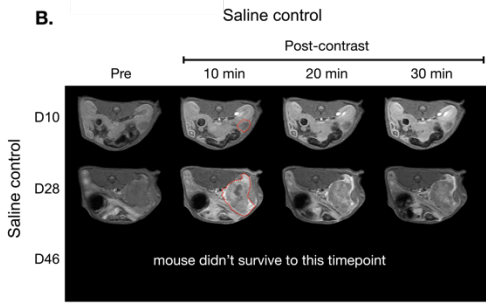


Figure 4. MT218-MRMI for monitoring tumor response to a mutated KRAS G12D peptide/R848/CpG neoantigen vaccine cocktail in C57BL/6 mice bearing orthotopic KPC-K8484 allografts. **A)** The experiment schedule for vaccine dosing and MRMI acquisitions. **B-E)** Representative T_1 -weighted 2D fast spin-echo axial MRMI images of the tumors (red dashed lines) of the mice treated saline (**B**) and the vaccine cocktail (**C-E**) before (Pre) and at 10, 20, and 30 min after intravenous injection of MT218 (0.1 mmol/kg, Post-contrast) during the experiment. **F)** Representative T_1 -weighted 2D fast spin-echo axial MRMI images of the normal pancreas in healthy mice. **G-K)** IHC and H&E staining of EDB-FN of the tumors or pancreatic tissues from the mice treated with saline (**G**), the vaccine (**H-J**) or normal pancreas (**H**). IF staining of $CD4^+$ (Alexa 488, green) and $CD8^+$ (Alexa 647, magenta) T cells in the tumors or pancreatic tissues from the mice treated with saline (**L**), vaccine (**M-O**), or normal pancreas (**P**).

Histological analysis of vaccine treated tissues at day 46 validated MRMI findings across response groups (**Figure 4H-J**). Non-responders showed large tumors with metastases, partial responders exhibited smaller tumors without metastases, and complete responders showed no detectable tumors. EDB-FN staining intensity correlated with MRMI enhancement patterns, with stronger staining in non-responder and partial responder tumors compared to complete responder pancreatic tissue. Complete responders maintained normal pancreatic architecture but showed uniform EDB-FN staining in sclerotic nodules, potentially indicating scarring or DAMP-mediated responses after tumor elimination (**Figure 4K**) [62]. Immunofluorescence revealed an immune-excluded TME in non-responding and partially responding tumors, with $CD4^+$ and $CD8^+$ T cells concentrated at the periphery (**Figure 4M, N**). Complete responders showed robust $CD4^+$ and $CD8^+$ T cell infiltration throughout pancreatic tissues.

Response assessment on day 28 demonstrated MT218-MRMI's predictive capability. Two distinct enhancement patterns emerged (**Figure 5A**): larger tumors with a strong rim and weak core enhancement (characteristic of partial responders) and smaller tumors with uniform strong enhancement (typical of complete responders). Histologically, responding tumors exhibited a scar-like tissue architecture with significant EDB-FN staining, whereas partial responders showed weaker EDB-FN expression (**Figure 5B**). Immunofluorescence revealed minimal $CD4^+$ cells at the tumor periphery and sparse $CD8^+$ cells in partial responders, in contrast to strong $CD4^+$ staining in scar-like tissues and substantial $CD4^+/CD8^+$ T cell accumulation throughout pancreatic tissues in responders (**Figure 5C**). These findings demonstrate MT218-MRMI's ability to detect distinct enhancement patterns within two weeks of treatment initiation, enabling early differentiation of

response patterns. Longitudinal assessment further refined response classification based on enhancement patterns, tumor progression, and therapeutic outcomes.

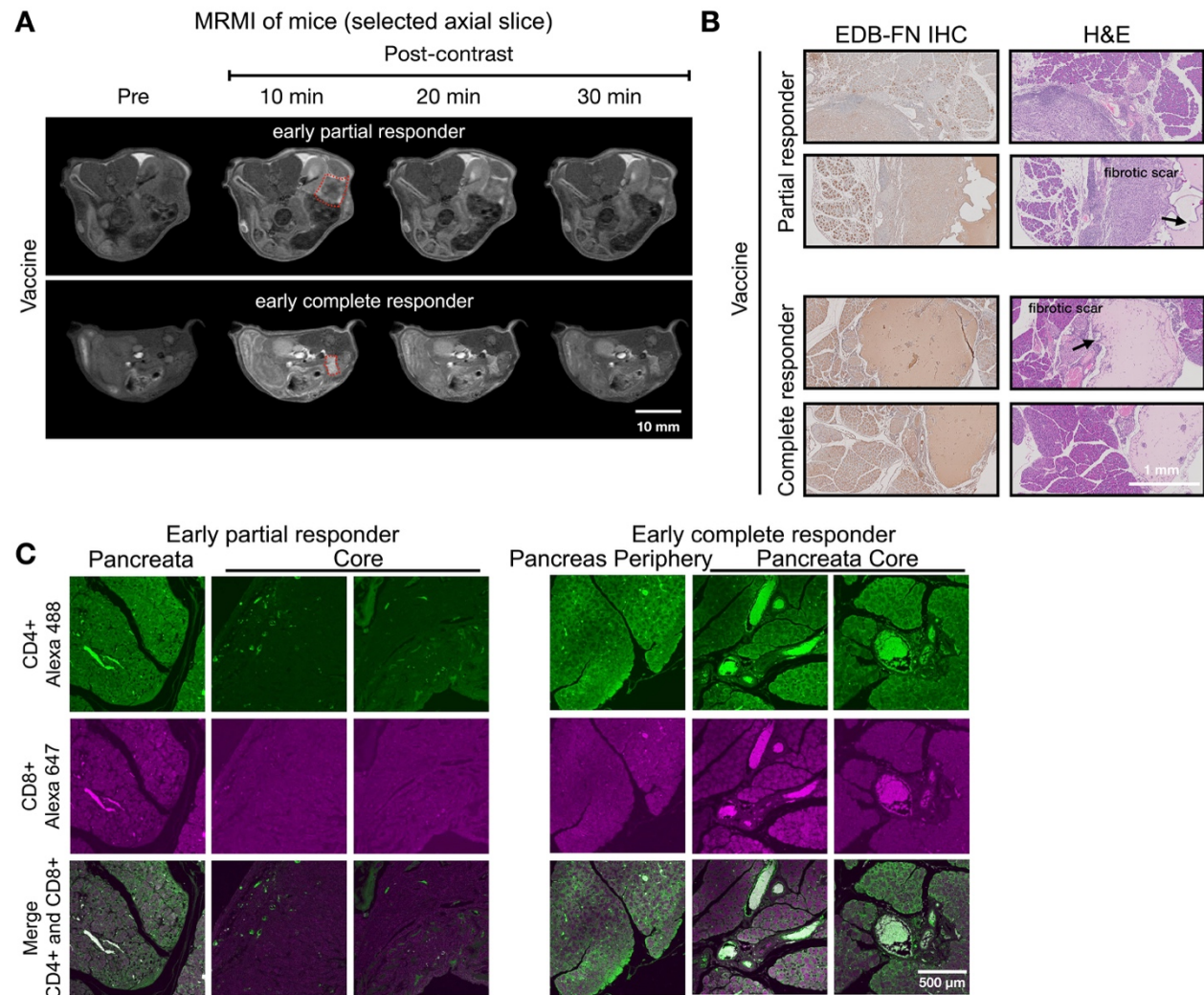


Figure 5. MT218-MRMI for monitoring early tumor response to a mutated KRAS G12D peptide/R848/CpG neoantigen vaccine cocktail in C57BL/6 mice bearing orthotopic KPC-K8484 allografts. B) Representative T₁-weighted 2D fast spin-echo axial MRMI images of tumors (red dashed lines) of the mice treated with the vaccine on day 28. Subtraction images are shown for signal difference between pre-contrast (Pre) and post-contrast at 10 min. B) IHC and H&E staining of the tumors. C) IF staining of CD4⁺ and CD8⁺ T cells in the tumors.

MT218-MRMI for monitoring and predicting tumor responses to combined treatments with vaccine and VISTA blockade

Building on our monotherapy findings, we next investigated MT218-MRMI's predictive capability in combination therapy using the vaccine cocktail with anti-VISTA mAb. Following the procedure outlined in **Figure 6A**, the PDAC tumor bearing mice received the initial vaccine on day 10 and a booster on day 17, alongside anti-VISTA mAb treatment (12 doses over 4 weeks, starting on day 12). MT218-MRMI revealed three distinct response patterns (**Figure 6B-E, Figure S9**). Non-responders (4 mice) developed large tumors with weak enhancement (2.74-fold CNR increase) on day 28, progressing to substantial growth with heterogeneous enhancement (3.80-fold CNR increase) and detectable metastases by day 46 (**Figure 6C, Figure S10**). Partial responders displayed reduced tumor volume (<30% compared to the control growth curve) with bright peripheral enhancement (4.51-fold CNR increase) on day 28. This was followed by tumor regrowth, characterized by distinctive rim signal enhancement and weak core enhancement (2.93-fold CNR) by day 46 (**Figure 6D, Figure S10**). Complete responders (13 mice) exhibited intense signal enhancement (6.94-fold CNR increase) at 10 minutes post-contrast on day 28 and achieved complete tumor resolution by day 46 (**Figure 6E, Figure S10**).

All mice were sacrificed and their tumors and pancreatic tissues were harvested following the final MRMI scan at day 46. The analyses tumor and pancreatic tissues by IHC, H&E and IF validated the findings from MT218-MRMI, **Figure 6F-M**. Complete responders had normal pancreatic tissue structure as compared to the complete responders treated with vaccine alone, **Figure 6I**. Non-responders and partial responders showed an immune-excluded TME, characterized by substantial CD4⁺ T cell presence throughout the tumors and limited CD8⁺ T cells at the tumor periphery with little to none in inner tumors (**Figure 6J, K**). In contrast, complete responders exhibited robust infiltration of both CD4⁺ and CD8⁺ T cells throughout pancreatic tissue (**Figure 6M**), confirming successful immune activation.

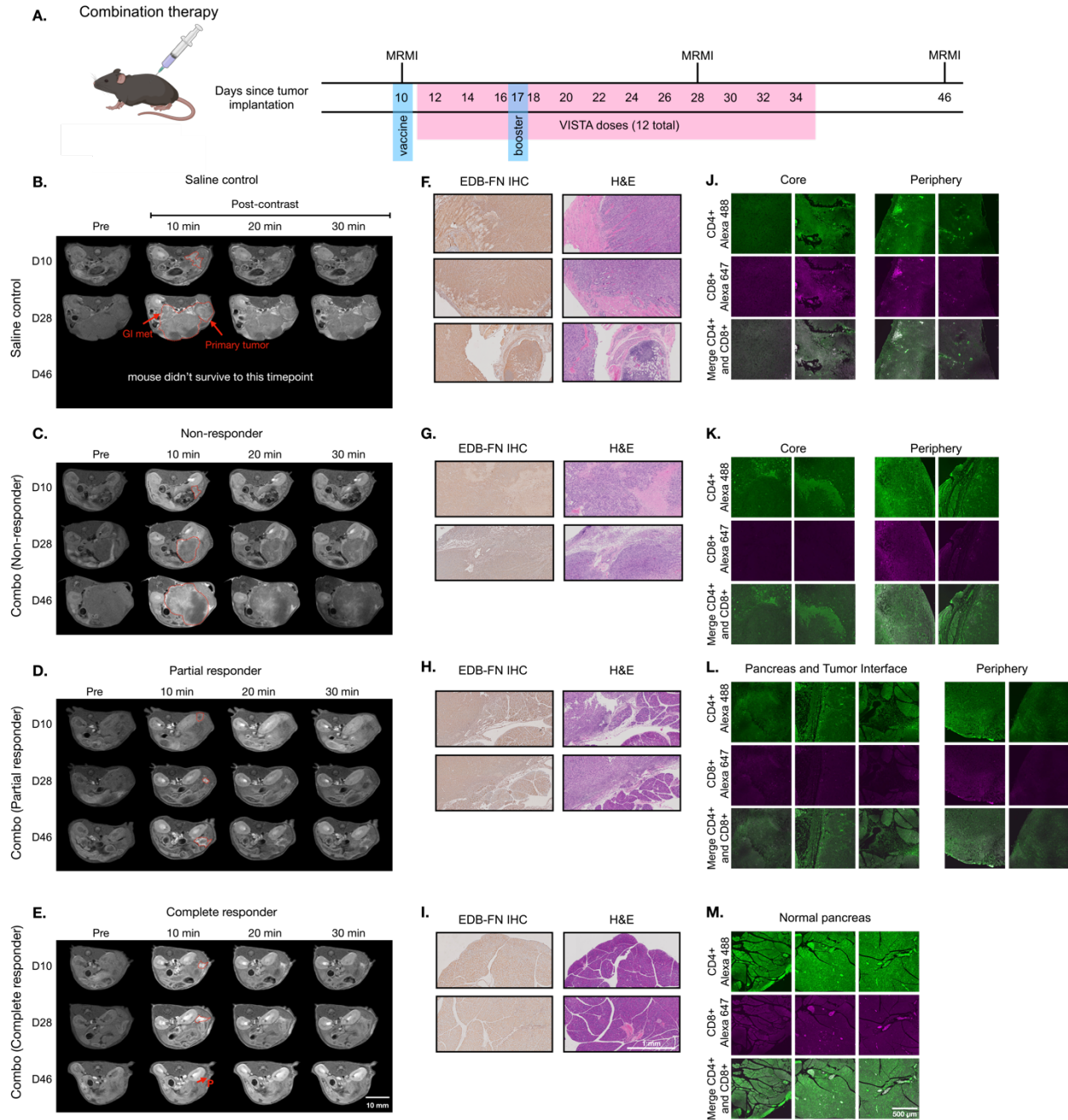


Figure 6. MT218-MRMI for monitoring tumor response to the combination therapy of the G12D peptide/R848/CpG neoantigen vaccine cocktail and anti-VISTA mAb in C57BL/6 mice bearing orthotopic KPC-K8484 allografts. A) The experiment schedule with vaccine dosing on day 10 and 17. B-E) Representative T₁-weighted 2D fast spin-echo axial MRMI images of the tumors (red dashed lines) of the mice treated saline (B) and the vaccine cocktail (C-E) before (Pre) and at various time points after intravenous injection of MT218 (0.1 mmol/kg, Post-contrast). F-I) IHC and H&E staining of EDB-FN of the tumors or pancreatic tissues from the mice treated with saline (F) or the vaccine (G-I). IF staining of CD4⁺ (Alexa 488, green) and CD8⁺ (Alexa

647, magenta) T cells in the tumors or pancreatic tissues from the mice treated with saline (**I**) and vaccine (**J-K**).

Figure 7 showed two distinct MT218-MRMI signal enhancement patterns on day 28 post-treatment: strong rim enhancement with weaker core enhancement in large tumors (early partial responders) and uniform strong enhancement across smaller tumors (early responders) at 10 min post-injection. These signal patterns are similar as those in vaccine treated tumors, **Figure 5**. IHC analysis confirmed that stronger MRMI signal enhancement correlated with higher EDB-FN expression (**Figure 7B**). Unlike vaccine-treated tumors, early responders showed no scar-like tissues (**Figure 7**). IF analysis demonstrated CD4⁺ and CD8⁺ T cell infiltration at tumor peripheries and pancreas-adenocarcinoma borders in partial responders (**Figure 7C**). Early responders exhibited robust CD4⁺ and CD8⁺ T cell presence throughout adenocarcinoma regions and adjacent pancreatic tissues. These findings demonstrate MT218-MRMI's capability to detect early immunotherapy responses through signal enhancement patterns and tumor size changes, making it an effective tool for monitoring tumor progression and treatment outcomes.

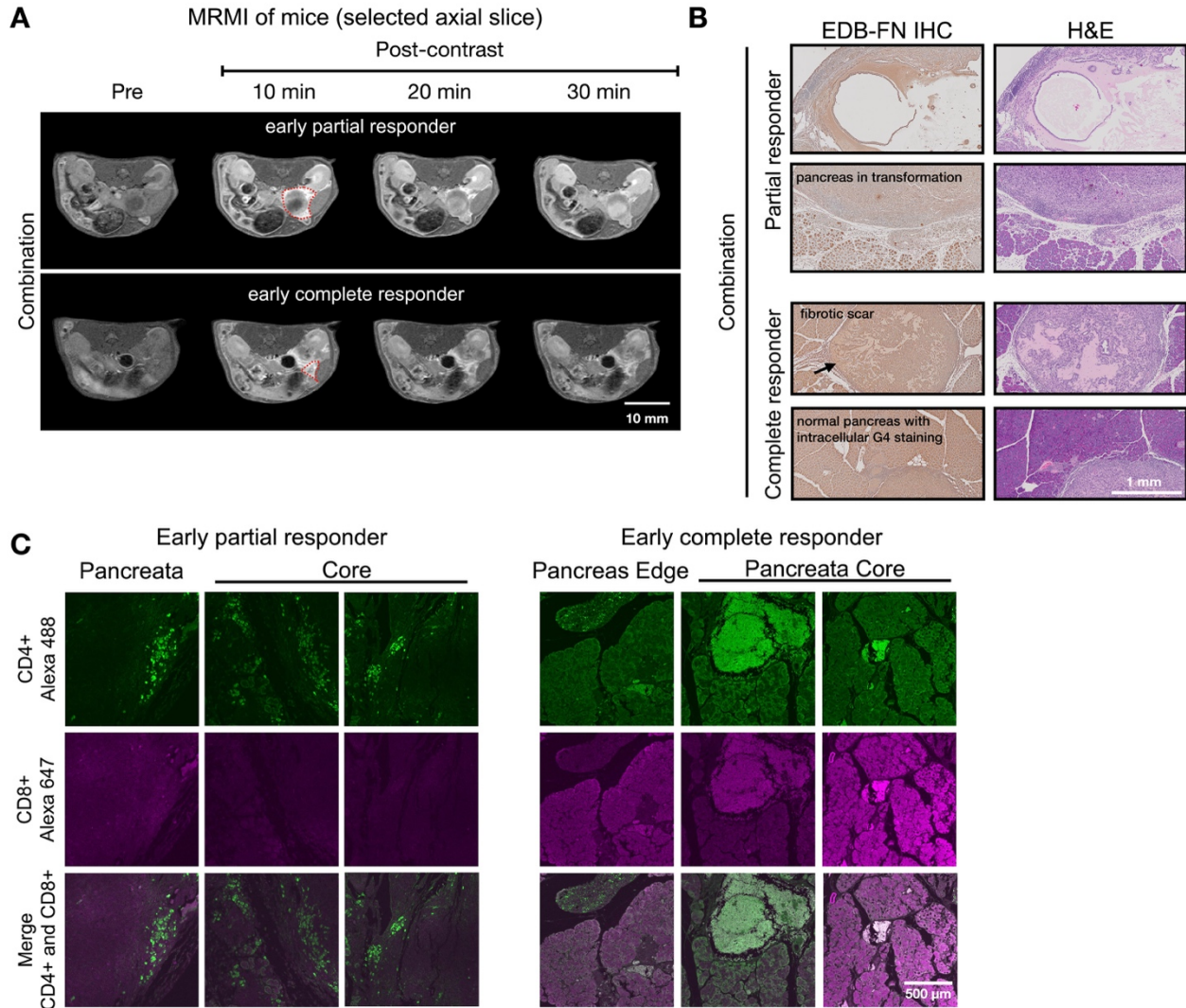


Figure 7. MT218-MRMI for monitoring early tumor response to anti-VISTA and mutated KRAS^{G12D} peptide/R848/CpG neoantigen vaccine cocktail in C57BL/6 mice bearing orthotopic KPC-K8484 allografts. B) Representative T₁-weighted 2D fast spin-echo axial MRMI of tumors (red dashed lines). Imaging of the mice treated with combination therapy was acquired on day 28. B) IHC and H&E staining of tumors. C) IF staining of CD⁴⁺ and CD⁸⁺ T cells in the tumors.

Predicting long-term therapeutic outcomes with MRMI

We developed a classification model based on Cox hazards regression and early-stage MT218-MRMI signal data to predict therapeutic outcomes in PDAC-bearing mice. Imaging analysis identified distinct response patterns characterized by signal enhancement and immune

characteristics that correlated with treatment outcomes. Non-responders exhibited low MRMI signal enhancement throughout tumors, corresponding to an immune-desert TME, rapid tumor growth, and metastasis. Stable disease cases showed bright tumor periphery with moderate core enhancement, reflecting an immune-excluded TME and rapid tumor growth without metastasis. Partial responders displayed bright tumor periphery with weaker core enhancement, also indicating an immune-excluded TME but with inhibited tumor growth and no metastasis. Complete responders demonstrated uniform bright enhancement throughout the tumor, correlating with an immune-inflamed TME and no detectable tumor or metastasis.

To validate this classification model, we analyzed a larger cohort of PDAC-bearing mice treated with saline (control), anti-VISTA mAb, vaccine, or combination therapy, evaluating MT218-MRMI's ability to detect early changes at 2 weeks post-treatment and predict long-term outcomes. The model achieved 82.9% overall accuracy in predicting tumor growth and survival outcomes, with treatment-specific accuracies of 100% for saline controls, 76.9% for vaccine treatment, and 71.4% for combination therapy. Notably, the model showed perfect prediction accuracy for both complete responders and non-responders (100%), though accuracy was lower for partial responders (22.2%).

Survival analysis extending to 200 days post-treatment revealed distinct patterns across treatment groups (**Figure 8**). Saline and anti-VISTA mAb groups showed no tumor-free survival (**Figure 8A**), while vaccine treatment achieved 43.2% overall disease-free survival, and combination therapy improved survival to 51.6%. When stratified by MT218-MRMI response categories, no tumor-free survival was observed in non-responders or stable disease groups across all treatments (**Figure 8B-D**). Partial responders achieved 24.2% disease-free survival with vaccine therapy (**Figure 8C**) and 27.3% with combination therapy (**Figure 8D**). Most significantly, complete responders in both vaccine and combination therapy groups maintained 100% tumor-free survival throughout the 200-day monitoring period, validating the predictive value of early MT218-MRMI signal patterns. Histological analysis of

These results demonstrate that MT218-MRMI effectively monitors tumor responses to immunotherapy through distinct enhancement patterns that correlate with immune activation, TME characteristics, and long-term survival outcomes. The high overall accuracy of the

classification model, particularly in identifying complete responders and non-responders, supports MT218-MRMI's potential as a predictive imaging tool for monitoring and predicting therapeutic outcomes to immunotherapies.

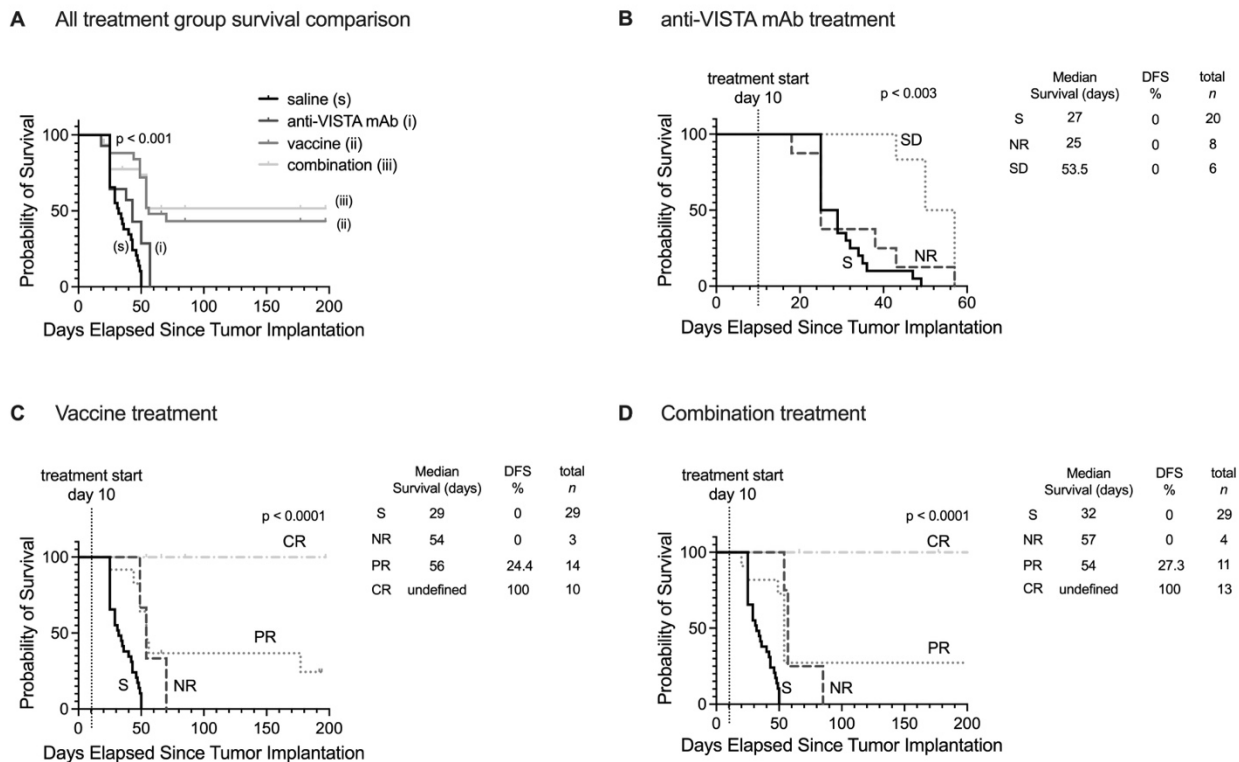


Figure 8. Predicting of therapeutic outcomes based on the responding criteria of MT218-MRMI. **A)** Kaplan-Meier curves of the overall survival of the mice bearing orthotopic KPC-K8484 PDAC of various treatment groups. **B-D)** Survival of the non-responders (NR), stable disease (SD), partial responders (PR), and complete responders (CR) based on MT218-MRMI in the anti-VISTA mAb group (**B**), the G12D peptide neoantigen vaccine cocktail group (**C**), and the vaccine cocktail + anti-VISTA mAb group with saline (S) as the control group.

DISCUSSION

Despite significant advances in immunotherapy, the effectiveness of existing clinical imaging tools for accurately and non-invasively assessing therapeutic response remains limited, particularly in pancreatic cancer. MRI provides high-resolution images of soft tissues and has been

used for PDAC detection [63]. However, it has not been utilized for assessing tumor response to immunotherapy or predicting therapeutic outcomes. Our previous studies demonstrated that MRMI of EDB-FN with MT218 is effective in detecting multiple aggressive cancers, including PDAC, and in monitoring tumor response to anticancer therapies in preclinical models [33, 48, 56], based on the role of EDB-FN in cancer EMT and invasion. This study further shows that MT218-MRMI of EDB-FN is effective in monitoring tumor responses to immunotherapy and predicting therapeutic outcomes in a preclinical PDAC model, leveraging its biological function as a lymphokine in the immune activation of T lymphocytes. Cellular FN, including EDB-FN, functions as an ECM protein that facilitates cell adhesion and migration. Both aggressive cancer cells and activated T cells secrete high levels of EDB-FN to promote invasion or migration, not by normal cells, providing a dynamic stromal marker for high-resolution MRMI to accurately detect aggressive tumors and monitor as well as predict responses to therapies, including immunotherapy [33, 41, 45].

MRMI offers unique advantages in characterizing dynamic TME changes through high-resolution imaging at any tissue depth, making it particularly valuable for visualizing pancreatic tumors often obscured by surrounding organs. MT218-MRMI provides high-resolution tumor imaging, revealing heterogeneous contrast enhancement patterns that reflect EDB-FN expression levels and distribution throughout immunotherapy treatment. MT218 generated strong signal enhancement 10–20 minutes post-injection, which gradually diminished over time. This gradual decline in signal intensity could be attributed to MT218's moderate binding affinity ($K_a = 3.5 \mu\text{M}$), diffusion, and clearance³⁸. However, no clear correlation between diffusion patterns and therapeutic outcomes could be established, as several factors may influence the agent's diffusion. For instance, intratumoral degradation of MT218's targeting peptide, ZD2, by ECM peptidases could accelerate its clearance. Additionally, tumor necrosis might affect the contrast agent's diffusion, leading to dynamic changes in enhancement patterns. Therefore, we focused on MRMI images taken 10 minutes post-injection, as they provided the most accurate representation of MT218 binding to EDB-FN for assessing tumor responses to immunotherapies.

The efficacy of immunotherapy depends on helper CD4⁺ and cytotoxic CD8⁺ T cells, with T cell distribution strongly correlating with both imaging patterns and survival outcomes (Spearman's $\rho = 0.83$, $p < 0.001$). Previous studies have established the multifunctional role of

oncofetal FN subtypes in T lymphocyte development, activation, and infiltration, with activated CD4⁺ and CD8⁺ T cells expressing and secreting high levels of EDB-FN [31, 36-40]. Studies by Wagner et al. showed that anti-CD3 activated CD4⁺ and CD8⁺ T cells expressed and resulted in high levels of EDB-FN exertion [45]. Our spatial and temporal analyses revealed distinct T cell distribution patterns corresponding to therapeutic response: non-responders showed characteristics of immune desert (limited T cell presence, mean density <50 cells/mm²), partial responders demonstrated immune exclusion phenotype (peripheral T cell accumulation, 245 ± 35 cells/mm² peripherally vs. 42 ± 12 cells/mm² centrally), and complete responders exhibited an inflamed immune phenotype (abundant intratumoral T cells, mean density 325 ± 45 cells/mm² throughout).

Analysis at day 28 showed responding tumors with significant CD4⁺ and CD8⁺ infiltration (>200 cells/mm²) either peripherally or throughout the tumor mass, correlating with MRMI enhancement patterns. By day 46, extensive CD4⁺ presence but limited CD8⁺ infiltration were seen in stable/partial responders. While specific CD4⁺ subtypes (Foxp3⁺ Tregs vs Foxp3⁻ helper cells) remain uncharacterized, enhanced MT218-MRMI signals likely reflect combined tumor and T cell EDB-FN secretion, providing a dynamic TME marker of therapeutic response. These imaging patterns corresponded with treatment outcomes, as demonstrated by Cox proportional hazards analysis showing significant survival benefits for both vaccine (HR = 0.43, 95% CI: 0.25-0.74, p = 0.002) and combination therapy (HR = 0.38, 95% CI: 0.22-0.66, p = 0.001) compared to saline controls. We speculate that the increased tumor signal enhancement in MT218-MRMI following immunotherapy may be associated with additional EDB-FN secretion by activated CD4⁺ and CD8⁺ T cells. Taken together, these results support the conclusion that the enhancement patterns detected by MT218-MRMI during immunotherapy reflect distinct types of tumor microenvironment in response to treatment (**Figure 9**).

Two weeks after therapeutic initiation

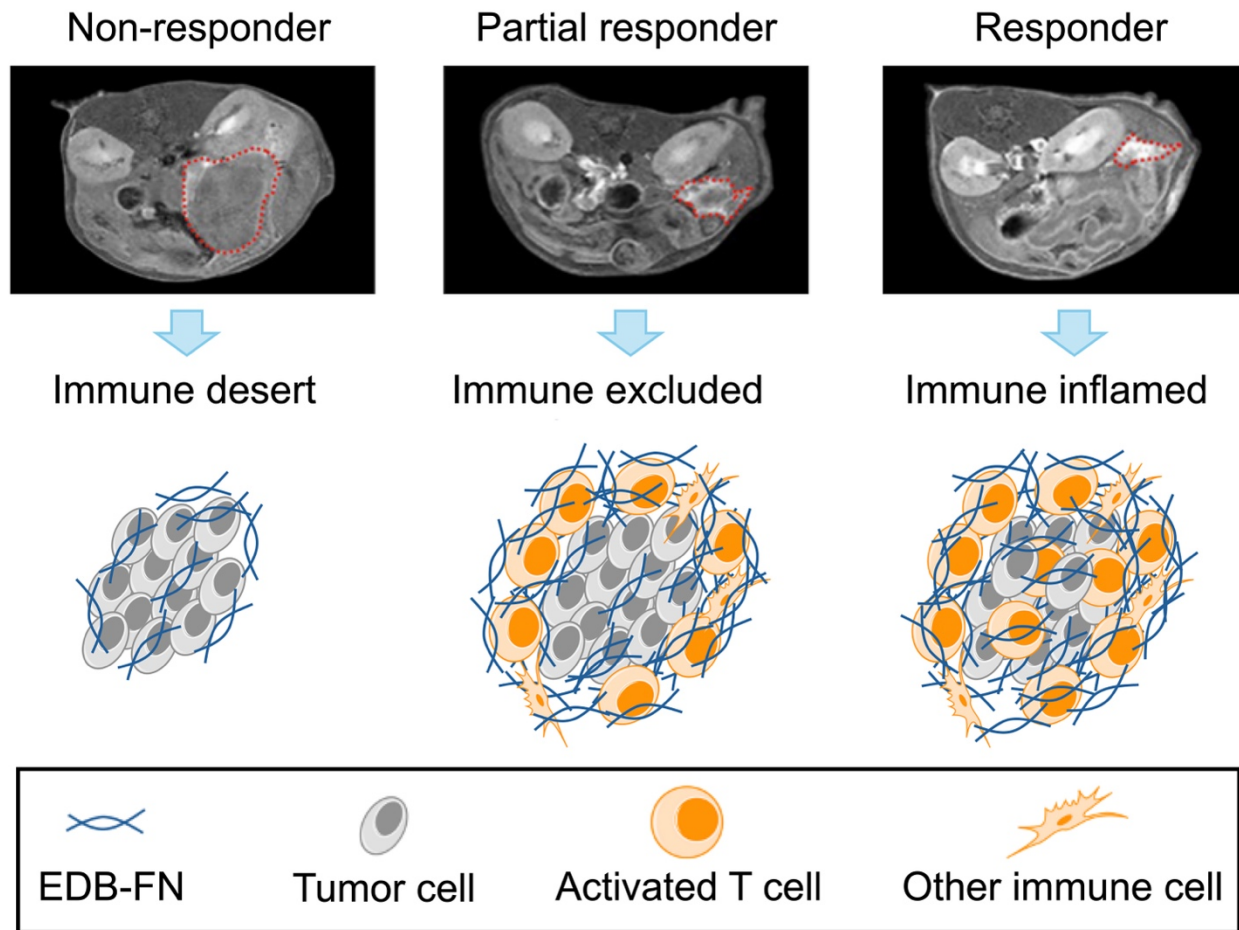


Figure 9. MT218-MRMI tumor signal enhancement patterns correlate with distinct immune tumor microenvironment (TME) phenotypes in immunotherapy response groups. MT218 contrast-enhanced MRMI images reveal heterogeneous signal enhancement patterns within tumors (indicated by red dashed lines), corresponding to immunotherapy responses in an orthotopic pancreatic cancer mouse model. These signal enhancement patterns reflect EDB-FN expression and correlate with three TME phenotypes: immune desert, immune excluded, and immune inflamed.

There have been significant efforts to develop molecular imaging tools for the biomarkers expressed on immune cell surface. Various PET probes have been developed for CD69 [64], CD8 [28, 65], fibroblast activation protein (FAP) [66], and immune checkpoints [67]. PET shows high sensitivity for molecular imaging of the biomarkers in preclinical and clinical studies. However, it is unable to provide visualization of the changes of TME phenotypes of the tumors in response to immunotherapy due to its spatial resolution. For example, PEI imaging of CD8⁺ T cells with a

zirconium-89-labeled one-armed antibody (89ZED88082A) was able to track CD8⁺ T cells, but unable to provide conclusive assessment of tumor response to immune checkpoint inhibitor in patients with colorectal cancer liver metastasis [28]. ⁶⁸Ga-FAPI PET/CT could provide accurate monitoring of the dynamic changes of CAFs and performed better than ¹⁸F-FDG PET for assessing tumor response to immune checkpoint inhibitor in patients with metastatic colorectal cancer [66]. Compared to PET, MR-based molecular imaging offers superior three-dimensional visualization of soft tissues. MT218-MRMI can effectively assess dynamic TME changes in high spatial resolution.

We have also demonstrated in this work that anti-VISTA mAb monotreatment prevented metastatic spread in KPC tumors and extended survival in stable disease, with significant improvement in survival probability (log-rank $p < 0.001$). The KRAS^{G12D} peptide vaccine improved survival (HR = 0.43, 95% CI: 0.25-0.74) and reduced tumor burden. While the combination of vaccine and anti-VISTA achieved optimal tumor-free survival (HR = 0.38, 95% CI: 0.22-0.66). The combination of anti-VISTA mAb and KRAS^{G12D} peptide vaccine demonstrated optimal therapeutic efficacy, preventing metastatic spread while achieving tumor-free survival in complete responders. Partial responders achieved median survival of 54-56 days compared to 27-32 days in non-responders, whereas complete responders did not reach median survival during the monitoring period. These results not only establish both the utility of MT218-MRMI for monitoring immunotherapy response but also demonstrate the therapeutic potential of combining checkpoint blockade with targeted vaccination in KRAS^{G12D}-mutated pancreatic cancer.

This investigation has several limitations. MRMI images and immunohistochemical/immunofluorescence stains were not perfectly co-registered due to tissue handling processes which resulted in tissue shrinkage and anatomical movement. These processing methods make it difficult to precisely correlate the MRMI data with activated T cells in the tumors. Future studies should consider the use of custom rigs in the MR bed and novel fixing methods to allow for better co-registration. In addition, MRMI could not differentiate activated CD4⁺ and CD8⁺ T cells in the tumors because both secrete EDB-FN. Our group is investigating the mechanisms that govern T cell secretion of EDB-FN. Moreover, we plan to further validate the effectiveness of MT218-MRMI with established immunotherapies, particularly vaccine adjuvants

in combination with clinically approved immune checkpoint inhibitors (ICIs), across multiple cancer types. Concurrent optimization of imaging intervals will be critical for maximizing early response prediction capabilities. Validation studies in larger cohorts encompassing diverse PDAC subtypes will be essential to establish the broader clinical utility of this imaging approach.

Outlook

MT218-MRMI demonstrates the capability for monitoring immunotherapy responses through semi-quantitative imaging in pancreatic cancer. As an FDA-approved agent for cancer detection currently under clinical investigation [57], MT218-MRMI enables high-resolution, non-invasive molecular imaging of the tumor microenvironment (TME), capturing treatment response heterogeneity. MT218-MRMI could provide early characterization of treatment responses, distinguishing non-responders, individuals with stable disease, partial responders, and complete responders, which is valuable to guide precision immunotherapy. Given the current lack of reliable predictive imaging tools for PDAC patients receiving immunotherapy, MT218-MRMI represents a significant advancement in image-guided treatment monitoring. Our findings establish MT218-MRMI as a promising platform for monitoring immunotherapy response in pancreatic cancer, warranting further clinical investigation and development. Successful clinical translation of MT218 could provide real-time, non-invasive assessment of therapeutic response and have a potential to transform clinical decision-making and ultimately improve patient outcomes.

METHODS

Cell Culture

Murine Kras^{G12D/+}; P53^{R172H/+}; Pdx1-Cre PDAC cells (KPC-K8484 or KPC), derived from an inducible murine model, were provided by Dr. Jordan Winter (The University Hospitals of Cleveland, OH). Cells were transfected with lentivirus to express GFP and Luciferin. Cells were cultured in an incubator at 37 °C and 5% CO₂ with normal RPMI media (RPMI medium (Gibco, Waltham, MA) supplemented with 10% fetal bovine serum (Gibco, Waltham, MA) and 1%

Penicillin/Streptomycin (Thermo Fisher Scientific)). Cells were split twice a week for a maximum of 12 passages to prevent significant genetic changes.

Animals care and tumor model establishment

Seven-week-old male and female C57BL/6 mice (The Jackson Laboratory, Bar Harbor, ME) were used for *in vivo* experimentation. Mice were housed in the Case Western Reserve University Small Animal Imaging Center, in accordance with IACUC approved animal manipulation protocols. To recapitulate the tumor microenvironment, therapy distribution conditions and contrast uptake preclinical tumors were implanted into the pancreas. KPC-GFP-Luc cells were implanted in mice via pancreatic laparotomy while mice were under anesthesia with 2% isoflurane (Covetrus, Portland, ME) and O₂ (1L/min). Orthotopic tumors were established whereby 5000 KPC cells suspended in a 30 μ L PBS-Matrigel mixture, at a 2:1 ratio, and were injected into the pancreas. Following a 10-day surgical recovery period, staples were removed from the mice and they were imaged in a 3.0T MRI MRS*DRYMAG (MR Solutions, Surrey UK), which established a baseline, prior to treatment, MRMI data set. Tumor treatment was initiated if tumors were clearly visualized and had reached sizes of $>20 \text{ mm}^3$. To validate implantation prior to MRMI, tumor growth was also monitored using bioluminescence imaging on a IVIS Spectrum (Perkin Elmer, Waltham, MA, USA). For preliminary and validation studies, mice were implanted with subcutaneous flank tumors with 100,000 KPC-GFP-Luc in a 1:1 PBS-Matrigel mixture. 100 μ L was injected into the flank and tumors were allowed to grow until they had reach 100 mm^3 before imaging was conducted.

Immunotherapy injections and formulation

Five distinct groups of mice were utilized for this study: negative control (no surgery), positive control (surgery, i.p. saline dosed as a imaging control based on past precedent), anti-VISTA mAb treated (ICI therapy, clone #13F3, BioXCell Inc, Lebanon, NH), peptide vaccine cocktail of (KRAS-G12D peptide (KLVVVGADGVGKSALTI) [5] (Atlantic Peptides, Concord,

NH) and TLR7/8/9 agonists, resiquimod (R848) and CpG-ODN Class B 1826 (InvivoGen, San Diego, CA), and the combination of anti-VISTA mAb and peptide vaccine cocktail. Intraperitoneal (i.p.) injections of 200 μ g anti-VISTA mAb were given to mice 3 times a week, at most every other day, to relevant groups beginning on day 12 after tumor initiation. The vaccine cocktail was administered at a dose of 25 μ g R848, 20 μ g G12D peptide, and 15 μ g CpG-ODN on day 10 (following MRMI, prior to ICI therapy) and 17 after tumor initiation. The combination treatments were performed by i.p. injections of anti-VISTA mAb and the vaccine cocktail with same doses and schedule as each individual treatment. Mice in the control group received equivalent volumes of saline at the same dosing schedule as the relevant treatment group.

Image acquisition

A 3.0T MRS*DRYMAG small animal scanner (MR Solutions, Surrey, UK) with a short mouse coil was used to acquire all images. Images were acquired at 4 timepoints: prior to contrast injection (pre-contrast), 10 minutes post-contrast injection (10 min), 20 minutes post-contrast injection (20 min), and 30 minutes post-contrast injection (30 min). At each timepoint a T_1 -weighted axial fast spin echo scan (T_1 w FSE; TE: 11 ms, TR: 305 ms, slice thickness: 1 mm, matrix: 256 x 256, 4 averages, flip angle: 90) and a 3D fast low angle shot (3D FLASH; TE: 3.8 ms, TR: 23 ms, slice thickness: 0.2 mm, matrix: 128 \times 256 \times 128, 2 averages, flip angle: 25°) based on reconstruction of coronal slices was acquired. Additionally, a non-contrast T_2 -weighted coronal FSE (TE: 68 ms, TR: 5000 ms, averages 1, slice thickness 1 mm) was acquired to measure tumor size and fluid content of the tumor cores, the peritumoral region, and the extratumoral space.

Image analysis

Region-of-interest (ROI) based image analysis was performed using FIJI open-source software and MATLAB software (GitHub, W.Z.). Pancreatic tumors were localized using the kidney and spleen as anatomical landmarks. Conventional contrast-to-noise ratio (CNR) analysis involved drawing ROIs of whole tumors, one muscle region that served as control normal tissue,

and background for noise. ROI analysis was performed for every slice of T₁-weighted axial images containing a pancreatic lesion. CNR was calculated using the following: $CNR = \frac{average\ signal_{tumor} - average\ signal_{muscle}}{\sigma_{noise}}$. CNR values were calculated for MRI acquired at all time points. Post-contrast CNR values were normalized to the pre-contrast value for comparison. To avoid bias, CNR calculations were performed independently by two individuals, one blinded. Images were adjusted to the same window and level based on muscle tissue for image subtraction. Segmentation for volume was also conducted via ITK SNAP and FIJI by collecting ROI measurements over the volume of the tumor. Volume measurements were conducted by two individuals, with at least one blinded.

For coronal image analysis of T₂w and FLASH scans, each coronal MRI sequence was interpolated into a three-dimensional scan and post processed in Horos and FIJI. ROIs were drawn around the spleen, liver, tumor, muscle, and background. CNR were calculated as described above. Three-dimensional scans were sliced along the Z-axis and the slice with average tumor enhancement was isolated.

Histological staining and grading

Following euthanasia, tumors, liver, kidneys and spleen were dissected and fixed in formalin for 24 hrs. Tissues were then stored in 70% ethanol and labelled in cassettes. Histological staining was conducted by the tissue resource core at the Case Cancer Comprehensive Center. Tissues were sectioned at 5 μm and fixed to coverslip slides. Hematoxylin and eosin (H&E) staining was conducted with the standard procedure. Immunohistochemistry (IHC) was performed using an anti-G4 mAb (Absolute Antibody, Boston, MA) at a ratio of 1:100. Briefly, after deparaffinization, antigen retrieval was performed at 125 °C for 30 s in pH = 6.0 citrate buffer, followed by blocking with 3% H₂O₂ peroxidase and Background Sniper (BioCare Medical, Pacheco, CA) for 8 and 20 min, respectively. Primary anti-G4 (for EDB-FN) antibody was incubated with tissue sections at RT for 1 hour with agitation. Primary antibody detection was performed with Mach 3 Rabbit detection solution (BioCare Medical) for 30 min. Visualization was performed with betazoid DAB (BioCare Medical, Pacheco, CA) for 5 min, followed by a 30

second counterstain with hematoxylin (BioCare Medical). Stained slides were imaged with a Bx61WS (Olympus, Waltham, MA) slide scanner and processed in the associated OlyVIA software. Histological interpretation was conducted by a board-certified pathologist blinded to sample groups.

Immunological assays

Dual immunofluorescence staining was performed on OCT-embedded tissue sections. Samples were brought to room temperature, washed twice with PBS to remove OCT, and a hydrophobic barrier was drawn around the tissue sections. The tissue was fixed with 100-200 μ L of ice-cold acetone per slide, incubated at -20 °C for 5-10 min, and washed three times with PBS. Blocking was performed for 30-60 min with 5% serum goat (Sigma-Aldrich, St. Louis, MO) in PBS-T (0.1% Tween-20 in PBS). A cocktail of primary antibodies with mouse reactivity, each raised in different species, was prepared in 1% serum in PBS-T. Primary antibodies targeting CD4⁺ and CD8⁺ (rat anti-CD4⁺ and rabbit anti-CD8⁺, Thermo Fisher Scientific, Waltham, MA) were applied to the tissue sections and incubated at room temperature for 1-2 hours, followed by overnight incubation at 4 °C in a humidified chamber. After washing with TBS-T, a cocktail of species-specific secondary antibodies conjugated to distinct fluorophores (Alexa Fluor 488 anti-rat and Alexa Fluor 647 anti-rabbit, Thermo Fisher Scientific) was applied to the sections and incubated in the dark at room temperature for 1-4 hours. Following secondary antibody staining, the slides were washed, mounted with DAPI-containing mounting medium (Thermo Fisher Scientific), and coverslipped. The slides were sealed with nail polish, dried for 5 min, and imaged. All slides were stored in the dark at 4 °C or -20 °C. Prepared slides were then imaged on an Olympus FluoView FV1000 confocal microscope (Olympus, Tokyo, Japan) at 10x magnification. Alexa 488 and Alexa 647 were imaged and set to green and magenta, respectively. Maximum signal was determined based on normal spleen sample and intensity was kept consistent amongst samples. Twelve slices were acquired between the range where cells were visible. Z-stacks were reconstructed at maximum intensity in MATLAB based on the acquired tiff files. Histogram analysis was conducted by thresholding CD4 and CD8 stained slides, which were all acquired

under the same confocal conditions. The images were thresholded prior to analysis and the ImageJ histogram feature was used to acquire pixel values.

Classification and survival analysis

The classification model was based on Cox proportional hazards regression using early-stage MT218-MRMI signal patterns. Images were acquired at 10 minutes post-injection, as this timepoint provided optimal visualization of MT218 binding to EDB-FN. Enhancement patterns were quantified using a semi-automated region-of-interest (ROI) analysis to calculate signal-to-noise ratios and enhancement distribution metrics (peripheral:core ratio, uniformity index). The classification model incorporated both quantitative imaging features and histologically confirmed immune characteristics to categorize responses as non-responder, stable disease, partial response, or complete response. Model performance was evaluated through leave-one-out cross-validation in a cohort of 41 PDAC-bearing mice treated with saline (n = 14), VISTA (n = 10), vaccine (n = 13), or combination therapy (n = 14). Kaplan-Meier survival analysis was performed with outcomes monitored for up to 200 days post-treatment, and statistical significance was assessed using log-rank tests. Hazard ratios (HR) with 95% confidence intervals (CI) were calculated to quantify treatment effects relative to saline controls. Classification accuracy was evaluated globally and by response category, with separate analyses for each treatment group to assess model robustness across different therapeutic interventions.

Statistical analysis

GraphPad Prism 9 and 10 were used for statistical analyses. Student's t-test (two-tailed, unpaired) was employed for categorical variables. Two-way ANOVAs with Tukey's post hoc test was used for longitudinal MRMI signal analysis between groups and for comparisons of outcomes between therapeutic groups. Kaplan-Meier analysis was utilized for survival studies. A two-sided $p < 0.05$ was considered statistically significant.

ACKNOWLEDGEMENTS

Acknowledgements: We thank all members of the Lu lab for engaging in many thoughtful discussions and providing critical feedback on this work. We thank Yang Yang and Yikun Wang previously of the Wang lab at Cleveland Clinic for their help in antibody purification and preliminary input on immunotherapy assays. We thank Dr. Jerky Ebai of the University Hospitals for his assistance in radiological reading. We thank Adam Kresak and Jenifer Mikulan from the Tissue Resources Shared Resource of the Case Comprehensive Cancer Center for their assistance with histopathologic (IHC, IF and H&E) staining. We also thank Abhinav P. Acharya from Department of Biomedical Engineering for valuable discussions about EDB-FN expression by activated T cells.

Funding Sources: This research was funded by National Cancer Institute of the National Institutes of Health grant R01 CA235152 (ZRL) as well as an NCI CURE Supplemental Award under the R01 CA235152 parent grant (ZRL), a CWRU subcontract of R44CA265626 (ZRL) from Molecular Theranostics, R01CA164225 (LLW), R01CA223804 (LLW), R21CA258618 (LLW), RSG-18-045-01-LIB from the American Cancer Society (LLW). Furthermore, work in this manuscript was supported by the Tissue Resources Shared Resource of the Case Comprehensive Cancer Center (P30CA043703).

Author contributions: Z.-R.L., V.L., and L.L.W. conceived the concept of the project, conducted data curation and wrote the manuscript. V.L. was involved in all aspects of the project, including experimental design and execution, data analysis, editing and writing. W.Z. analyzed data, created code to assist in MRMI data analysis and provided editorial assistance. I.H. performed mouse experiments, helped write the methods, analyzed data, and provided editing assistance. E.H. performed mouse experiments and analyzed data. J.D. and E.D. provided critical materials and assisted in experimental design. R.C.H. provided input on experimental design and provided editing assistance. K.W.B. performed animal surgeries for pancreatic tumor establishment. X.Y. analyzed MRMI data. H.G. read and graded slides for histopathological assessment. R.K. and J.W. provided materials and personnel for experimentation and also provided

key scientific input about pancreatic cancer and the clinical landscape. L.L.W. provided for key materials, designed experiments and provided immunological interpretation of results. Z-R. L. supervised the study, obtained funding, editing and data curation.

Competing interests: The authors declare the following competing interests: The Z-R. L. and R.C.H. have ownership interest in Molecular Theranostics, LLC., which is developing the contrast agent MT218. L.L.W is involved in the commercial development of VISTA with ImmuNext Inc. Corporation (Lebanon, NH, USA).

REFERENCES

1. Korman AJ, Garrett-Thomson SC, Lonberg N. The foundations of immune checkpoint blockade and the ipilimumab approval decennial. *Nat Rev Drug Discov.* 2022; 21: 509-28.
2. Kubli SP, Berger T, Araujo DV, Siu LL, Mak TW. Beyond immune checkpoint blockade: emerging immunological strategies. *Nat Rev Drug Discov.* 2021; 20: 899-919.
3. Bialkowski L, van Weijnen A, Van der Jeught K, Renmans D, Daszkiewicz L, Heirman C, et al. Intralymphatic mRNA vaccine induces CD8 T-cell responses that inhibit the growth of mucosally located tumours. *Sci Rep.* 2016; 6: 22509.
4. Cafri G, Gartner JJ, Zaks T, Hopson K, Levin N, Paria BC, et al. mRNA vaccine-induced neoantigen-specific T cell immunity in patients with gastrointestinal cancer. *J Clin Invest.* 2020; 130: 5976-88.
5. Pan J, Zhang Q, Palen K, Wang L, Qiao L, Johnson B, et al. Potentiation of Kras peptide cancer vaccine by avasimibe, a cholesterol modulator. *EBioMedicine.* 2019; 49: 72-81.
6. Pant S, Wainberg ZA, Weekes CD, Furqan M, Kasi PM, Devoe CE, et al. Lymph-node-targeted, mKRAS-specific amphiphile vaccine in pancreatic and colorectal cancer: the phase 1 AMPLIFY-201 trial. *Nat Med.* 2024; 30: 531-42.
7. Demaria O, Cornen S, Daeron M, Morel Y, Medzhitov R, Vivier E. Harnessing innate immunity in cancer therapy. *Nature.* 2019; 574: 45-56.
8. Wang L, Rubinstein R, Lines JL, Wasiuk A, Ahonen C, Guo Y, et al. VISTA, a novel mouse Ig superfamily ligand that negatively regulates T cell responses. *J Exp Med.* 2011; 208: 577-92.
9. Xu W, Hieu T, Malarkannan S, Wang L. The structure, expression, and multifaceted role of immune-checkpoint protein VISTA as a critical regulator of anti-tumor immunity, autoimmunity, and inflammation. *Cell Mol Immunol.* 2018; 15: 438-46.
10. Roy D, Gilmour C, Patnaik S, Wang LL. Combinatorial blockade for cancer immunotherapy: targeting emerging immune checkpoint receptors. *Front Immunol.* 2023; 14: 1264327.
11. Zhang K, Zakeri A, Alban T, Dong J, Ta HM, Zalavadia AH, et al. VISTA promotes the metabolism and differentiation of myeloid-derived suppressor cells by STAT3 and polyamine-dependent mechanisms. *Cell Rep.* 2024; 43: 113661.
12. Xu W, Dong J, Zheng Y, Zhou J, Yuan Y, Ta HM, et al. Immune-Checkpoint Protein VISTA Regulates Antitumor Immunity by Controlling Myeloid Cell-Mediated Inflammation and Immunosuppression. *Cancer Immunol Res.* 2019; 7: 1497-510.
13. Flies DB, Wang S, Xu H, Chen L. Cutting edge: A monoclonal antibody specific for the programmed death-1 homolog prevents graft-versus-host disease in mouse models. *J Immunol.* 2011; 187: 1537-41.
14. Wang L, Le Mercier I, Putra J, Chen W, Liu J, Schenk AD, et al. Disruption of the immune-checkpoint VISTA gene imparts a proinflammatory phenotype with predisposition to the development of autoimmunity. *Proc Natl Acad Sci U S A.* 2014; 111: 14846-51.
15. Le Mercier I, Chen W, Lines JL, Day M, Li J, Sergeant P, et al. VISTA Regulates the Development of Protective Antitumor Immunity. *Cancer Res.* 2014; 74: 1933-44.

16. Liu J, Yuan Y, Chen W, Putra J, Suriawinata AA, Schenk AD, et al. Immune-checkpoint proteins VISTA and PD-1 nonredundantly regulate murine T-cell responses. *Proc Natl Acad Sci U S A*. 2015; 112: 6682-7.
17. Ta HM, Roy D, Zhang K, Alban T, Juric I, Dong J, et al. LRIG1 engages ligand VISTA and impairs tumor-specific CD8(+) T cell responses. *Sci Immunol*. 2024; 9: eadi7418.
18. Mehta N, Maddineni S, Kelly RL, Lee RB, Hunter SA, Silberstein JL, et al. An engineered antibody binds a distinct epitope and is a potent inhibitor of murine and human VISTA. *Sci Rep*. 2020; 10: 15171.
19. Moon TJ, Ta HM, Bhalotia A, Paulsen KE, Hutchinson DW, Arkema GM, et al. Nanoparticles targeting immune checkpoint protein VISTA induce potent antitumor immunity. *Journal for ImmunoTherapy of Cancer*. 2024; 12: e008977.
20. Wang L, Jia B, Claxton DF, Ehmann WC, Rybka WB, Mineishi S, et al. VISTA is highly expressed on MDSCs and mediates an inhibition of T cell response in patients with AML. *Oncoimmunology*. 2018; 7: e1469594.
21. Gao J, Ward JF, Pettaway CA, Shi LZ, Subudhi SK, Vence LM, et al. VISTA is an inhibitory immune checkpoint that is increased after ipilimumab therapy in patients with prostate cancer. *Nat Med*. 2017; 23: 551-5.
22. Blando J, Sharma A, Higa MG, Zhao H, Vence L, Yadav SS, et al. Comparison of immune infiltrates in melanoma and pancreatic cancer highlights VISTA as a potential target in pancreatic cancer. *Proc Natl Acad Sci U S A*. 2019; 116: 1692-7.
23. Kakavand H, Jackett LA, Menzies AM, Gide TN, Carlino MS, Saw RPM, et al. Negative immune checkpoint regulation by VISTA: a mechanism of acquired resistance to anti-PD-1 therapy in metastatic melanoma patients. *Mod Pathol*. 2017; 30: 1666-76.
24. Gordon-Weeks A, Yuzhalin AE. Cancer Extracellular Matrix Proteins Regulate Tumour Immunity. *Cancers (Basel)*. 2020; 12.
25. Robertson C, Sebastian A, Hinckley A, Rios-Arce ND, Hynes WF, Edwards SA, et al. Extracellular matrix modulates T cell clearance of malignant cells in vitro. *Biomaterials*. 2022; 282: 121378.
26. Ortiz-Munoz G, Brown M, Carbone CB, Pechuan-Jorge X, Rouilly V, Lindberg H, et al. In situ tumour arrays reveal early environmental control of cancer immunity. *Nature*. 2023; 618: 827-33.
27. Tsuzuki T, Ohe C, Osawa T, Yasuda Y, Tanaka T, Anai S, et al. Prognostic value of immune phenotype and PD-L1 status in recurrent or metastatic renal cell carcinoma: an exploratory analysis of the ARCHERY study. *Pathology*. 2023; 55: 31-9.
28. Kist de Ruijter L, van de Donk PP, Hooiveld-Noeken JS, Giesen D, Elias SG, Lub-de Hooge MN, et al. Whole-body CD8(+) T cell visualization before and during cancer immunotherapy: a phase 1/2 trial. *Nat Med*. 2022; 28: 2601-10.
29. Sun R, Limkin EJ, Vakalopoulou M, Dercle L, Champiat S, Han SR, et al. A radiomics approach to assess tumour-infiltrating CD8 cells and response to anti-PD-1 or anti-PD-L1 immunotherapy: an imaging biomarker, retrospective multicohort study. *Lancet Oncol*. 2018; 19: 1180-91.
30. Hynes RO, Yamada KM. Fibronectins: multifunctional modular glycoproteins. *J Cell Biol*. 1982; 95: 369-77.

31. Crisa L, Cirulli V, Ellisman MH, Ishii JK, Elices MJ, Salomon DR. Cell adhesion and migration are regulated at distinct stages of thymic T cell development: the roles of fibronectin, VLA4, and VLA5. *J Exp Med*. 1996; 184: 215-28.
32. Nourmohammadi F, Forghanifard MM, Abbaszadegan MR, Zarrinpour V. EZH2 regulates oncomiR-200c and EMT markers in esophageal squamous cell carcinomas. *Sci Rep*. 2022; 12: 18290.
33. Laney V, Hall R, Yuan X, Hampson E, Halle A, Yeung G, et al. MR Molecular Image Guided Treatment of Pancreatic Cancer with Targeted ECO/miR-200c Nanoparticles in Immunocompetent Mouse Tumor Models. *Pharm Res*. 2024.
34. Lemanska-Perek A, Adamik B. Fibronectin and its soluble EDA-FN isoform as biomarkers for inflammation and sepsis. *Adv Clin Exp Med*. 2019; 28: 1561-7.
35. Godfrey HP. T cell fibronectin: an unexpected inflammatory lymphokine. *Lymphokine Res*. 1990; 9: 435-47.
36. Mizobata S, Tanimura H, Yamaue H, Tani M, Tsunoda T, Iwahashi M, et al. Fibronectin promotes the proliferation of cytotoxic T lymphocytes generated from cancer patients. *Br J Cancer*. 1996; 74: 1598-604.
37. Ybarrondo B, O'Rourke AM, McCarthy JB, Mescher MF. Cytotoxic T-lymphocyte interaction with fibronectin and vitronectin: activated adhesion and cosignalling. *Immunology*. 1997; 91: 186-92.
38. Davis LS, Oppenheimer-Marks N, Bednarczyk JL, McIntyre BW, Lipsky PE. Fibronectin promotes proliferation of naive and memory T cells by signaling through both the VLA-4 and VLA-5 integrin molecules. *J Immunol*. 1990; 145: 785-93.
39. Nojima Y, Humphries MJ, Mould AP, Komoriya A, Yamada KM, Schlossman SF, et al. VLA-4 mediates CD3-dependent CD4+ T cell activation via the CS1 alternatively spliced domain of fibronectin. *J Exp Med*. 1990; 172: 1185-92.
40. Fernandes NRJ, Reilly NS, Schrock DC, Hocking DC, Oakes PW, Fowell DJ. CD4(+) T Cell Interstitial Migration Controlled by Fibronectin in the Inflamed Skin. *Front Immunol*. 2020; 11: 1501.
41. Hall RC, Vaidya AM, Schiemann WP, Pan Q, Lu ZR. RNA-Seq Analysis of Extradomain A and Extradomain B Fibronectin as Extracellular Matrix Markers for Cancer. *Cells*. 2023; 12.
42. Vaidya A, Wang H, Qian V, Gilmore H, Lu ZR. Overexpression of Extradomain-B Fibronectin is Associated with Invasion of Breast Cancer Cells. *Cells*. 2020; 9.
43. Qiao PL, Gargasha M, Liu Y, Laney VEA, Hall RC, Vaidya AM, et al. Magnetic resonance molecular imaging of extradomain B fibronectin enables detection of pancreatic ductal adenocarcinoma metastasis. *Magn Reson Imaging*. 2022; 86: 37-45.
44. Hauzenberger D, Martin N, Johansson S, Sundqvist KG. Characterization of lymphocyte fibronectin. *Exp Cell Res*. 1996; 222: 312-8.
45. Wagner C, Burger A, Radsak M, Blum S, Hug F, Hansch GM. Fibronectin synthesis by activated T lymphocytes: up-regulation of a surface-associated isoform with signalling function. *Immunology*. 2000; 99: 532-9.
46. Hemmerle T, Probst P, Giovannoni L, Green AJ, Meyer T, Neri D. The antibody-based targeted delivery of TNF in combination with doxorubicin eradicates sarcomas in mice and confers protective immunity. *Br J Cancer*. 2013; 109: 1206-13.

47. Mohammadgholi M, Sadeghzadeh N, Erfani M, Abediankenari S, Abedi SM, Emrarian I, et al. Human Fibronectin Extra-Domain B (EDB)-Specific Aptide (APTEDB) Radiolabelling with Technetium-99m as a Potent Targeted Tumour-Imaging Agent. *Anticancer Agents Med Chem*. 2018; 18: 277-85.
48. Vaidya A, Ayat N, Buford M, Wang H, Shankardass A, Zhao Y, et al. Noninvasive assessment and therapeutic monitoring of drug-resistant colorectal cancer by MR molecular imaging of extradomain-B fibronectin. *Theranostics*. 2020; 10: 11127-43.
49. Saw PE, Xu X, Kang BR, Lee J, Lee YS, Kim C, et al. Extra-domain B of fibronectin as an alternative target for drug delivery and a cancer diagnostic and prognostic biomarker for malignant glioma. *Theranostics*. 2021; 11: 941-57.
50. Ayat NR, Qin JC, Cheng H, Roelle S, Gao S, Li Y, et al. Optimization of ZD2 Peptide Targeted Gd(HP-DO3A) for Detection and Risk-Stratification of Prostate Cancer with MRI. *ACS Med Chem Lett*. 2018; 9: 730-5.
51. Li Y, Gao S, Jiang H, Ayat N, Laney V, Nicolescu C, et al. Evaluation of Physicochemical Properties, Pharmacokinetics, Biodistribution, Toxicity, and Contrast-Enhanced Cancer MRI of a Cancer-Targeting Contrast Agent, MT218. *Invest Radiol*. 2022; 57: 639-54.
52. Lu ZR, Laney V, Li Y. Targeted Contrast Agents for Magnetic Resonance Molecular Imaging of Cancer. *Acc Chem Res*. 2022; 55: 2833-47.
53. Qiao P, Ayat NR, Vaidya A, Gao S, Sun W, Chou S, et al. Magnetic Resonance Molecular Imaging of Extradomain B Fibronectin Improves Imaging of Pancreatic Cancer Tumor Xenografts. *Front Oncol*. 2020; 10: 586727.
54. Vaidya A, Shankardass A, Buford M, Hall R, Qiao P, Wang H, et al. MR Molecular Imaging of Extradomain-B Fibronectin for Assessing Progression and Therapy Resistance of Prostate Cancer. *Chem Biomed Imaging*. 2024; 2: 560-8.
55. Laney V, Hall R, Yuan X, Hampson E, Halle A, Yeung G, et al. MR Molecular Image Guided Treatment of Pancreatic Cancer with Targeted ECO/miR-200c Nanoparticles in Immunocompetent Mouse Tumor Models. *Pharm Res*. 2024; 41: 1811-25.
56. Nicolescu C, Kim J, Sun D, Lu ZR. Assessment of the Efficacy of the Combination of RNAi of lncRNA DANCR with Chemotherapy to Treat Triple Negative Breast Cancer Using Magnetic Resonance Molecular Imaging. *Bioconjug Chem*. 2024; 35: 381-8.
57. Li Y, Apseloff G, Tweedle MF, Gao S, Henry E, Lu ZR. Pharmacokinetics and Tolerability of the Cancer-Targeting MRI Contrast Agent MT218 in Healthy Males. *Invest Radiol*. 2024; 59: 165-9.
58. Ye J, Mills BN, Qin SS, Garrett-Larsen J, Murphy JD, Uccello TP, et al. Toll-like receptor 7/8 agonist R848 alters the immune tumor microenvironment and enhances SBRT-induced antitumor efficacy in murine models of pancreatic cancer. *J Immunother Cancer*. 2022; 10.
59. Okada H, Takahashi K, Yaku H, Kobiyama K, Iwaisako K, Zhao X, et al. In situ vaccination using unique TLR9 ligand K3-SPG induces long-lasting systemic immune response and synergizes with systemic and local immunotherapy. *Sci Rep*. 2022; 12: 2132.
60. Prokhnevskaya N, Cardenas MA, Valanparambil RM, Sobierajska E, Barwick BG, Jansen C, et al. CD8(+) T cell activation in cancer comprises an initial activation phase in lymph nodes followed by effector differentiation within the tumor. *Immunity*. 2023; 56: 107-24 e5.
61. Xie Q, Ding J, Chen Y. Role of CD8(+) T lymphocyte cells: Interplay with stromal cells in tumor microenvironment. *Acta Pharm Sin B*. 2021; 11: 1365-78.

62. Bhattacharyya S, Varga J. Endogenous ligands of TLR4 promote unresolving tissue fibrosis: Implications for systemic sclerosis and its targeted therapy. *Immunol Lett.* 2018; 195: 9-17.
63. Farr KP, Moses D, Haghighi KS, Phillips PA, Hillenbrand CM, Chua BH. Imaging Modalities for Early Detection of Pancreatic Cancer: Current State and Future Research Opportunities. *Cancers (Basel).* 2022; 14.
64. Edwards KJ, Chang B, Babazada H, Lohith K, Park DH, Farwell MD, et al. Using CD69 PET Imaging to Monitor Immunotherapy-Induced Immune Activation. *Cancer Immunol Res.* 2022; 10: 1084-94.
65. Tavare R, Danton M, Giurleo JT, Makonnen S, Hickey C, Arnold TC, et al. Immuno-PET Monitoring of Lymphocytes Using the CD8-Specific Antibody REGN5054. *Cancer Immunol Res.* 2022; 10: 1190-209.
66. Li K, Liu W, Yu H, Chen J, Tang W, Wang J, et al. 68Ga-FAPI PET imaging monitors response to combined TGF-betaR inhibition and immunotherapy in metastatic colorectal cancer. *J Clin Invest.* 2024; 134.
67. Bouleau A, Lebon V, Truillet C. PET imaging of immune checkpoint proteins in oncology. *Pharmacol Ther.* 2021; 222: 107786.

Graphic Abstract

MRMI monitoring tumor response to immunotherapy

